Nano Energy 83 (2021) 105772

Contents lists available at ScienceDirect

Nano Energy

journal homepage: http://www.elsevier.com/locate/nanoen

Full paper

Constructing high-rate and long-life phosphorus/carbon anodes for potassium-ion batteries through rational nanoconfinement

Wei Xiao [a,b], Xifei Li [a,b,*], Bin Cao [a,b], Gang Huang [a,b], Chong Xie [a,b], Jian Qin [a,b], Huijuan Yang [a,b], Jingjing Wang [a,b], Xueliang Sun [a,b,c,*]

[a] Xi'an Key Laboratory of New Energy Materials and Devices, Institute of Advanced Electrochemical Energy & School of Materials Science and Engineering, Xi'an University of Technology, Xi'an, Shaanxi 710048, China
[b] Shaanxi International Joint Research Center of Surface Technology for Energy Storage Materials, Xi'an, Shaanxi 710048, China
[c] Department of Mechanical and Materials Engineering, University of Western Ontario, London, ON N6A 5B9, Canada

ARTICLE INFO

Keywords:
Potassium-ion batteries
Phosphorus/carbon anode
Nanoconfinement
Pseudocapacitive behavior
Reaction mechanism

ABSTRACT

The development of stable and durable phosphorus anodes for potassium-ion batteries (PIBs) has been retarded by a sluggish reaction kinetics and a notorious volume change with an ambiguous reaction mechanism upon cycling. Herein, the phosphorus nanoparticles have been rationally encapsulated into a commercial porous carbon through an evaporation-condensation strategy. Benefitted from the improved structural integrity/stability of electronically/ionically insulating phosphorus in a conductive/robust carbon matrix with abundant K^+/electron migration channels, the phosphorus/carbon anode material with an appropriate phosphorus content (59.4 wt%) would achieve a large initial charging capacity of 744 mA h g^{-1} at 100 mA g^{-1} and a highly reversible capacity of 212 mA h g^{-1} at 3200 mA g^{-1} over 10,000 cycles with a superior rate capability of 287 mA h g^{-1} at 11,200 mA g^{-1}. Simultaneously, the electrochemical importance of phosphorus loading on potassium storage capability of derived phosphorus/carbon composites was also uncovered. Critically, the noticeable capacitive intercalation/extraction of K^+ in carbon nanostructure would significantly boost the charge storage process and promote the electrochemical performance of phosphorus/carbon anode. In terms of reaction mechanism for phosphorus/carbon anode, the active phosphorus would prefer to proceed a potassiation below 0.5 V upon discharging and a depotassiation below 1.0 V upon charging, accompanied by a reversible emergence/decomposition of K_4P_3. This novel study shedding lights on nanostructure design and mechanism clarification of phosphorus anode would contribute to the development of high-energy and long-life PIBs in practical applications.

1. Introduction

Confronting with an ever-increasing serious environmental pollution in parallel with a rapid depletion of traditional fossil fuel, lithium-ion batteries (LIBs), as the predominant power enablers for consumer electronics in last decades, have been proposed to drive the electric vehicles (EVs) and store the renewable energy in smart grids [1,2]. However, the geologically scarce lithium reserves, accompanied by the rocketing prices of lithium resources in the forecasted huge demand on transportation electrification and grid construction, have stimulated the continuous pursuits of sustainable, affordable, and reliable energy storage systems utilizing replaced charge carriers with an excellent working safety, a high energy density, and a long operating durability [3]. While the sodium-ion batteries (SIBs) were firstly revisited, the potassium-ion batteries (PIBs) have been further developed for natural abundance and environmental benignity of potassium resources without toxicity [4–7]. In earth's crust, the elemental content of potassium can reach 1.5 wt%, which is almost 900 times higher than that of lithium (0.0017 wt%), dramatically reducing the manufacturing cost of PIBs with potential applications in large-scale energy storage [6–8]. Compared with negative standard potentials for Li/Li^+ (−3.04 V) and Na/Na^+ (−2.71 V) vs. Standard Hydrogen Electrode (S.H.E.), a desirable redox potential of K/K^+ at −2.93 V (vs. S.H.E) could promise a high operating voltage and a considerable energy density [6–8]. Additionally,

* Corresponding authors at: Xi'an Key Laboratory of New Energy Materials and Devices, Institute of Advanced Electrochemical Energy & School of Materials Science and Engineering, Xi'an University of Technology, Xi'an, Shaanxi 710048, China.
E-mail addresses: xfli@xaut.edu.cn (X. Li), xsun9@uwo.ca (X. Sun).

https://doi.org/10.1016/j.nanoen.2021.105772
Received 14 September 2020; Received in revised form 14 December 2020; Accepted 10 January 2021
Available online 13 January 2021

the relatively weaker Lewis acidity for K^+ than those for Li^+ and Na^+ could obviously favor the formation of smaller solvated compounds with a higher ionic conductivity in electrolyte, while a low desolvation energy of K^+ would further accelerate its diffusion across electrode/electrolyte interface, leading to an exceptional rate capability [5]. Unfortunately, the shift of charge carrier from Li^+ to K^+ with the increases of atomic mass (6.94 vs. 39.1 g mol^{-1}) and ionic radius (76 vs. 138 pm) would inevitably diminish the reaction kinetics in electrodes and subsequently challenge their structure stability upon huge volume variation during the potassiation/depotassiation, further deteriorating the electrochemical reversibility and durability of PIBs [9,10]. Therefore, it is still necessary to rationally design and construct a stable yet efficient host material with abundant ion diffusion and electron transport channels for overcoming the sluggish solid-state diffusion and accommodating the repeated intercalation/extraction of large-sized K^+.

In terms of anode materials, the potassium metal was instantly denied as a safe anode for PIBs, due to its extremely low melting point (63.3 °C), violent reactivity toward electrolytes, and unavoidable dendrite formation upon potassium plating/stripping [8]. The development of suitable anode materials has been concentrating on the conventional graphite anode, which can reversibly intercalate Li^+ and K^+ with the generation of thermodynamically stable graphite intercalation compounds (GICs) [11,12]. Ji's group has firstly revisited the room-temperature intercalation of K^+ into layer-structured graphite anode through liquid electrolyte with a large reversible capacity of 273 mA h g^{-1} in the formation of KC_8 upon potassiation [13], which was later confirmed by Komaba and colleagues [14]. Interestingly, this breakthrough has further inspired the successful applications of various carbon materials, including graphitic carbon [15,16], disordered carbon [17,18], and soft carbon [19,20], as highly reversible and durable anodes for PIBs. Although different heteroatom doping approaches [21–27], rational nanostructure designs [28–31], and defect engineering [32] have been sucessively employed to boost the electrochemical performances of carbon anode materials, their reversible capacities and cycle life can hardly satisfy the stringent requirements in building high-energy PIBs for large-scale grid energy storage. At the same time, substantial efforts have been devoted to developing high-capacity alloy-type (tin-based [35–37], antimony-based [38–41], bismuth-based [42–44], etc.) and conversion-type (oxides [45–47], sulfides [48–51], selenides [52–55], nitride [56], etc.) anode materials for PIBs. Even though the combination of nanostructured anode materials with highly conductive carbon could partially alleviate the poor electrical conductivity and severe structural instability upon cycling, their reversible capacities still cannot exceed 600 mA h g^{-1} with a limited electrochemical durability below 200 cycles at a low current density, while the relatively high operating voltage range would further decrease the practical energy densities for these anode materials.

Particularly, the commercially available and relatively stable red phosphorus (P), which used to be recognized as a promising anode material of LIBs and SIBs for its ultrahigh theoretical capacity (2596 mA h g^{-1}) and a desirable redox potential (< 0.6 V) in a three-electron alloying reaction [57–61], has recaptured the scientific interests from electrochemical energy storage field as a competitive anode material for PIBs [62–64]. The first attempt on designing phosphorus-based anode materials for PIBs has been made by Zaiping Guo and colleagues for Sn_4P_3/C composite with a good reversible capacity and an acceptable cycle life [65]. However, the notorious large volume expansion/-shrinkage of phosphorus upon potassiation/depotassiation in multi-electron alloying/dealloying reactions would continuously shaken its inner structure stability, then trigger the gradual collapse of active materials, and ultimately generate the electrode pulverization, resulting in a continuous depletion of electrolyte upon solid electrolyte interphase (SEI) formation and a rapid capacity degradation upon cycling. Worse still, an inferior electrical conductivity for red P ($\sim 10^{-14}$ S cm^{-1}) would obviously increase the electrochemical polarization and reduce the utilization of active phosphorus, further compromising its rate capability [64]. To buffer the huge volumetric change and facilitate the electron/ion migrations during electrochemical reactions, the red P has been either mechanically milled with conductive carbon materials (graphite [66,67], porous carbon [68,69], carbon composites [70], etc.), or chemically combined with electrochemical inactive materials (CoP [71,72], FeP [73–75], etc.) and electrochemically active materials (GeP_5 [76], Sn_4P_3 [77,78], SnP_3 [79], Se-P [80,81], etc.). Admittedly, the downsized phosphorus particles with a weakened mechanical stress and an improved structural stability would have abundant short pathways for electron transport and ion diffusion, the highly active phosphorus composites with rich surface defects and large surface areas would induce their severe parasitic reactions with reactive electrolytes/ambient air and further sacrifice the electrochemical activity/reversibility upon discharging/charging processes [68]. At the same time, an evaporation-condensation strategy, which could spontaneously introduce sublimed phosphorus vapor into highly conductive/robust/-flexible carbon matrixes through capillary force and pressure difference, has been developed to accommodate the large volume variation and facilitate electron/ion migrations upon alloying/dealloying of phosphorus anodes [82–89]. The similar nanoconfinements of phosphorus have also been undertaken in various carbon nanostructures, including activated carbon [90], carbon nanotube-backboned mesoporous carbon [91], reduced graphene oxide [92], three-dimensional carbon nanosheet framework [93], N-doped porous hollow carbon nanofibers [94], hollow carbon [95], etc. Specifically, the strikingly different alloying reactions between phosphorus and potassium would determine the theoretical capacities (865 mA h g^{-1} for KP, 1154 mA h g^{-1} for K_4P_3, and 2596 mA h g^{-1} for K_3P) and volume expansion rates (232% for KP, 293% for K_4P_3, and 593% for K_3P) of discharged phosphorus anode materials. Intriguingly, Xu's group reported the formation of KP in the discharged phosphorus/carbon (P/C) electrode with a first charge capacity of 715 mA h g^{-1} at 100 mA g^{-1} (based on the content of red P) [93], while a discharged product of K_4P_3 was observed during the potassiation of phosphorus filled in N-doped porous hollow carbon nanofibers, yielding a large initial reversible capacity of 805 mA h g^{-1} at 100 mA g^{-1} with an 81% capacity retention after 100 cycles [94]. Furthermore, Zaiping Guo's group uncovered the emergence of K_3P in the potassiation of Sn_3P_4 anode and achieved a stable capacity of 403 mA h g^{-1} at 50 mA g^{-1} over 200 cycles in KFSI-based electrolyte [78]. Concurrently, the critical effects of phosphorus loading in derived composites on the physicochemical and electrochemical properties of phosphorus-based anode materials have chronically been ignored in the previous research works. Moreover, the larger ionic size for K^+ than that for Na^+ and Li^+ would severely challenge the structural integrity/stability of phosphorus anode materials with a huge volume change upon multi-electron alloying/dealloying reactions and further demand the rational designs of robust/conductive/porous/inexpensive carbon nanostructure to cushion the huge volumetric expansion/shrinkage of phosphorus upon discharging/charging. To further boost the electrochemical properties of phosphorus anode materials, it is also imperative to clarify the underlying potassium storage mechanism and make the utmost of active phosphorus in advanced carbon nanostructures upon potassiation/depotassiation toward a large reversible capacity, a long cycle life, an excellent rate capability, and a high energy density.

In this regard, we have rationally confined the red P nanoparticles into a commercially available and inexpensive porous carbon with a high surface area and a large pore volume through a facile evaporation-condensation route. This highly conductive and porous carbon matrix would not only offer abundant electron transport pathways for electrically/ionically insulating phosphorus nanoparticles, but also guarantee their convenient access to electrolyte with an exceptional K^+ diffusion capability. Simultaneously, the tremendous internal mechanical strain produced in huge volume change of phosphorus nanoparticles upon potassiation/depotassiation can be greatly relieved by this flexible and porous carbon nanostructure without structural collapse and electrode fracture. Benefitted from the significantly improved electronic/ionic

conductivities and outstanding structural integrity/stability, the P/C composite with an appropriate loading of phosphorus in porous carbon could proceed the efficient alloying/dealloying reactions with the reversible emergence/decomposition of K_4P_3, leading to a large initial charge capacity of 744 mA h g^{-1} at 100 mA g^{-1} and a highly reversible capacity of 212 mA h g^{-1} at 3200 mA g^{-1} after 10,000 cycles. With the assistance of a noticeable pseudocapacitive behavior, this P/C composite could further achieve a superior rate capability of 287 mA h g^{-1} at 11,200 mA g^{-1}. Concurrently, the underlying reaction mechanism of P/C anode upon potassiation/depotassiation was also revealed by electrochemical and spectroscopic characterizations. The outstanding electrochemical properties for this P/C composite with a low manufacturing cost and a high industrial scalability could open up a strategic avenue for developing high-capacity and long-life anode materials for high-energy PIBs.

2. Experimental

2.1. Materials synthesis

The porous carbon (Ketjen Black, EC600JD, Lion Speciality Chemicals Co. LTD.) was firstly hand grinded with commercial red P (98.5%, Aladdin Industrial Co. LTD.) in agate mortar for 10 min and then sealed in a quartz tube under vacuum. Importantly, the mixture in a sealed capsule was initially heated at 500 °C for 6 h at a heating rate of 2 °C min^{-1} to fully sublime the red P and further kept at 300 °C for 24 h at a cooling rate of 1 °C min^{-1} to efficiently convert condensational white phosphorus to stable red P. The as-synthesized P/C composite was carefully collected in an Ar-filled glove box, subsequently washed by carbon disulfide to eliminate residual white phosphorus and water/ethanol to remove impurities. After driing at 60 °C for 12 h in a vacuum oven, the P/C composite was immediately collected and stored in a Ar-filled glove box to prevent its surface oxidation in ambient air[68]. Specifically, the as-obtained P/C composite, thermally derived from the pristine mixture in a mass ratio of 1:1, 2:1, and 4:1 for red P to porous carbon, was denoted as P-C-1, P-C-2, and P-C-4, respectively.

2.2. Physical characterizations

The crystalline structures for P/C composites and discharged products were analyzed by X-ray Diffraction (XRD) utilizing a Bruker D8 Advance (Cu-Kα source, 40 kV, 40 mA) spectrometer, and the Raman scattering spectra were recorded by a Horiba Scientific LabRAM HR evolution spectrometer using a 532 nm laser at room temperature. Meanwhile, a Thermo Fisher ESCALAB Xi^+ instrument was employed to identify the elemental compositions and valence states of P/C composites by X-ray photoemission spectroscopy (XPS). The Thermogravimetric Analysis (TAG) experiments were further conducted by a Mettler Toledo TG-DSC Simultaneous Thermal Analyzer. Additionally, the nitrogen adsorption/desorption isotherms with the corresponding pore size distributions were performed by a Micromeritics ASAP 2460 Accelerated Surface Area and Porosimetry System. Moreover, the morphologies of P/C composites were observed by a Zeiss Gemini 300 scanning electron microscope (SEM) operated at 5 keV, while a JEOL JEM-F200 (HR) Field Emission Transmission Electron Microscope (TEM) equipped with an energy-dispersive X-ray spectrometer (EDX) was applied to study the microstructures and elemental mappings.

2.3. Electrochemical measurements

In the fabrication of P/C electrodes, 70 wt% P/C composite as active material, 15 wt% acetylene black as conductive agent, and 15 wt% sodium alginate (MP Biomedicals) as polymer binder were manually mixed and then dissolved into a suitable amount of water. The as-obtained homogeneous slurry was subsequently casted onto copper foil as current collector, further dried at 60 °C overnight in a vacuum oven, finally punched into ½ inch pellets with an average mass loading of ~ 1.0 mg cm^{-2} for active material. The conventional 2032-type coin cells in a half-cell configuration, consisting of a fresh potassium metal as anode, a polypropylene membrane (Celgard 2400) as separator, and a P/C electrode as cathode in liquid electrolyte, were assembled in an Ar-filled glove box to investigate the electrochemical properties of P/C composites. In this case, the liquid electrolyte was composed of 1.0 M KFSI in a mixing solution of ethylene carbonate (EC) and diethyl carbonate (DEC) with a volume ratio of 1:1. The electrochemical behaviors were characterized by cyclic voltammetry (CV) applying a Princeton ParSTAT MC 2000A electrochemical station at different scanning rates, while the galvanostatic charge/discharge performances were further evaluated by a Neware CT4000 battery testing system between 0.001 and 2.5 V (vs. K/K^+) at various current densities under room temperature. The galvanostatic intermittent titration (GITT) measurements were carried out by discharging/charging the cell for 10 min at a current density of 50 mA g^{-1} with a subsequent 2 h relaxation at an open-circuit state. Particularly, all specific capacities were calculated based on the total weight of P/C composite.

3. Results and discussions

The preparation of P/C composites following a typical evaporation-condensation method, as illustrated in Fig. 1, initiated from the uniform mixing of pristine phosphorus with porous carbon, then conducted a complete sublimation of red P under vacuum at 500 °C, subsequently proceeded a gradual condensation of phosphorus vapor in porous carbon above 300 °C through capillary force, and further undertook a long-lasting conversion from volatile white phosphorus to stable red P at 300 °C. Additionally, the as-obtained P/C composites were carefully washed by carbon disulfide solvent to eliminate residual white phosphorus and water/ethanol to remove impurities before vacuum drying and immediately transferred into an Ar-filled glove box for storage to inhibit the surface oxidation [68]. To investigate the effects of phosphorus loading on electrochemical properties, different mass ratios of red P to porous carbon (1:1, 2:1, and 4:1) in the pristine mixture were adopted in the fabrication of P/C composites (P-C-1, P-C-2, and P-C-4).

To confirm the coexistence of phosphorus and carbon in various P/C composites, the XRD was primarily employed to identify their microstructures, as shown in Fig. 2(a). When it comes to pristine red P, an obvious peak around 15.3° and a broad peak around 34.0° can be separately indexed to (013) and (31−8) diffraction planes for monoclinic phosphorus (JCPDS No. 00-044-0906, space group of *P*2/*c*) with a medium-range ordered structure [83,96]. In terms of various P/C composites, the (013) and (31−8) peaks would firstly appear with a diminished intensity and then sharpen with an enhanced intensity, signifying the efficient confinement of phosphorus into porous carbon and effective preservation of phosphorus features. In addition, the gradual emergences of (11−7), (−218), and (026) peaks at 27.4°, 30.8°, and 31.3° further proved the formation of crystalline red P in derived composites after thermal treatments, while this dominant phase in P/C composites would become more obvious with an increase of initial content for phosphorus in the pristine mixture with porous carbon [97–99]. The similar results were also observed by Raman spectra in Fig. 2(b). Specifically, a series of features in the range of 300–500 cm^{-1} should be attributed to P–P bonding in pristine red P, while two sharp peaks at 1338 and 1594 cm^{-1} separately corresponded to a D band of sp^3 disordered structure and a G band of sp^2 graphitic phase in amorphous porous carbon [68,100–103]. Interestingly, both carbon and phosphorus features can be retained in derived materials, further verifying the concurrence of phosphorus and carbon in P/C composites. The increase of peak intensities for phosphorus features in Raman spectra conforms to the sharpening tendency of phosphorus characteristics in XRD patterns for P/C composites, hinting at a gradual increase of phosphorus loading. As seen by full survey XPS for different P/C composites in Fig. 2(c), the phosphorus and carbon elements coexisted in derived materials with the

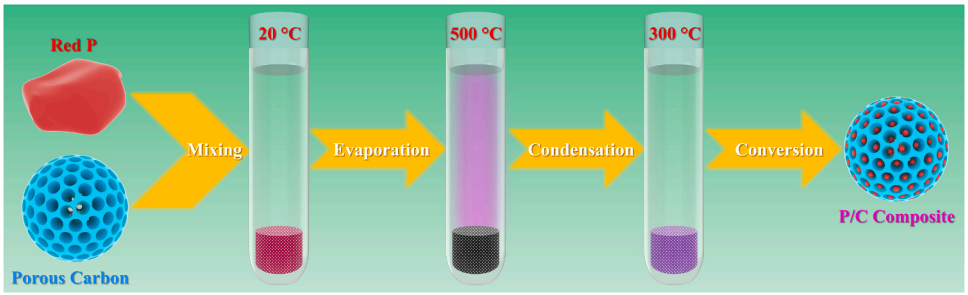

Fig. 1. Schematic diagram of synthesis procedure for P/C composite.

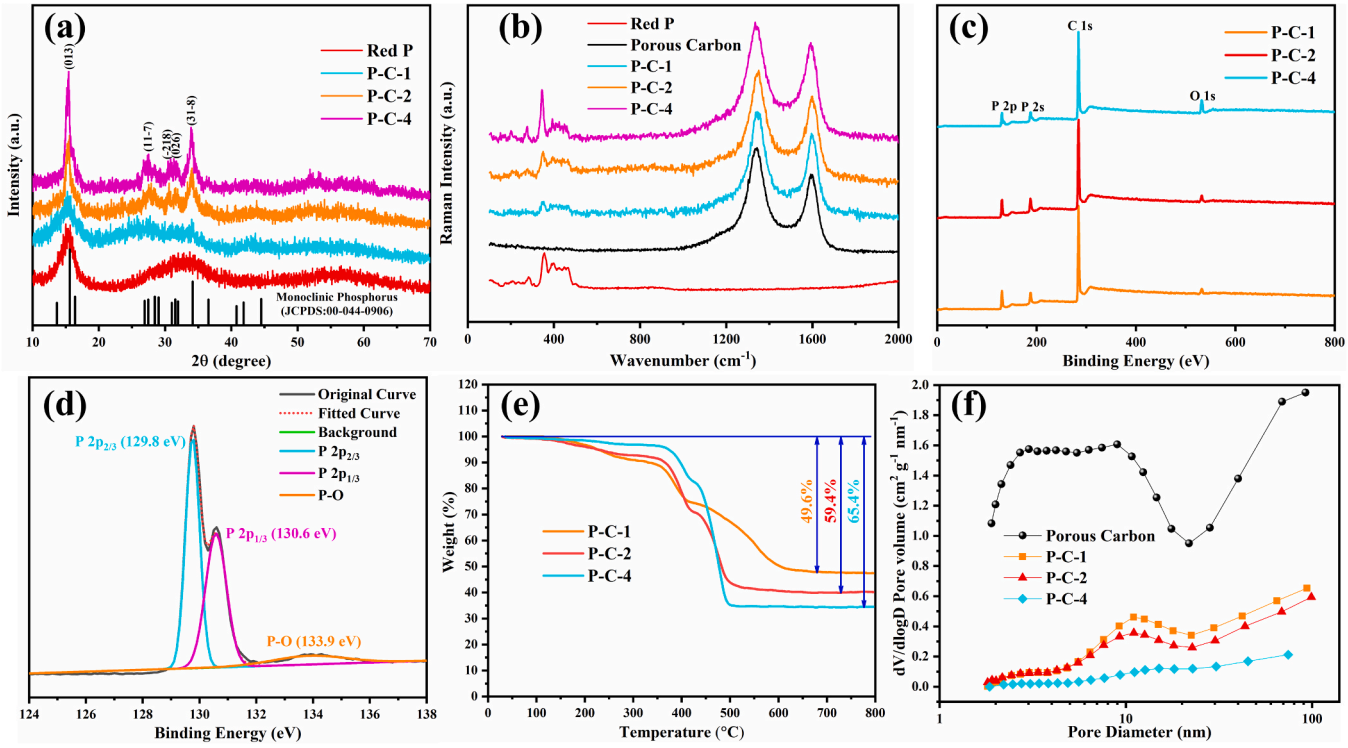

Fig. 2. Physical properties for various P/C composites. (a) XRD patterns for red P and different P/C composites. (b) Raman spectra for red P, porous carbon, and different P/C composites. (c) The full survey XPS for different P/C composites. (d) The high-resolution P 2p XPS for P-C-2. (e) TGA results for different P/C composites. (f) Pore size distributions for porous carbon and different P/C composites.

negligible oxygen contaminations. Furthermore, the high-resolution P 2p XPS for P-C-2 in Fig. 2(d) could be deconvoluted into three peaks, involving a strong peak at 129.8 eV for P–P bonding in P $2p_{2/3}$ feature, a noticeable peak at 130.6 eV for P–P bonding in P $2p_{1/3}$ characteristic, and a weak peak at 133.9 eV for P–O bonding. The similar peak-fittings of P 2p XPS for P-C-1 and P-C-4 can also be found in Supporting information (Figs. S1 and S2). According to TGA results in Fig. 2(e), the phosphorus contents for P-C-1, P-C-2, and P-C-4 were determined as 49.6 wt%, 59.4 wt%, and 65.4 wt%, respectively, which are consistent with previous findings in XRD patterns and Raman spectra for different P/C composites. Moreover, the Brunauer–Emmett–Teller (BET) surface area and total pore volume would apparently decrease from 1765.4 m^2 g^{-1}/3.04 cm^3 g^{-1} for porous carbon to 182.1 m^2 g^{-1}/0.77 cm^3 g^{-1} for P-C-1, 161.9 m^2 g^{-1}/0.72 cm^3 g^{-1} for P-C-2, and 37.9 m^2 g^{-1}/0.25 cm^3 g^{-1} for P-C-4. Considering the obvious type-IV characteristics for nitrogen adsorption/desorption isotherms in Fig. S3 with a small hysteresis loop at a medium-pressure range, the porous carbon should possess a large amount of mesopores, which was further identified by Barrett–Joyner–Halenda (BJH) pore size distributions in Fig. 2(f) [96]. Appealingly, the huge pore volumes for mesopores in the size range of 2.0–10 nm were notably reduced upon loading phosphorus into porous carbon, implying the efficient encapsulation of phosphorus nanoparticles into mesopores. Importantly, the rich mesopores in porous carbon would not only ensure a facile electrolyte permeation and enable a rapid ion diffusion across electrode/electrolyte interface, but also accommodate the huge volume change of phosphorus upon potassiation through large inner void spaces. Even though the phosphorus nanoparticles can be both encapsulated into mesopores [84,104,105] and micropores [87,106] for carbon nanomaterials, the effective nanoconfinement of phosphorus into micropores would require an energy-consuming vaporization process at the very high temperature (~ 900 °C) to promise an efficient diffusion of phosphorus vapor into limited microporous structures [87,106]. Conversely, the mesopores featured with a huge surface area and a large internal space could easily absorb more phosphorus nanoparticles through a strong capillary force and an obvious pressure difference, effectively accommodate the large volume change of phosphorus nanoparticles upon potassiation/depotassiation, and further ensure a rapid permeation of liquid electrolyte across electronically/ionically insulating phosphorus, leading to a superior electrochemical performance of phosphorus/carbon anode.

Meanwhile, the SEM and TEM techniques were also applied to observe the morphologies and structures of different P/C composites for validating the successful confinement of red phosphorus into porous carbon. Compared with the pristine carbon nanomaterials with an average diameter of 30–50 nm in Fig. S4, the as-obtained P/C nanoparticles with an even distribution barely changed their shapes and sizes in Fig. 3(a–f), manifesting the effective retention of conductive carbon matrix without destructing the porous nanostructure after phosphorus impregnation. Regardless of a partial nanoparticle agglomeration in Fig. 3(g) for P-C-2, the pristine porous and conductive frameworks in irregular shapes can still be reserved upon loading phosphorus into porous carbon. With the assistance of scanning transmission electron microscopy (STEM) in Fig. 3(h and i) and the corresponding EDX mappings in Fig. 3(j and k), the carbon and phosphorus elements were found to be uniformly distributed in the composite of P-C-2, implying a homogeneous elemental combination of phosphorus with carbon.

Furthermore, the CV tests in Fig. 4(a–c) with a voltage range of 0.001–2.5 V (vs. K/K^+) at a scan rate of 0.2 mV s^{-1} were conducted to understand the influences of different phosphorus loadings on the electrochemical behaviors of various P/C composites. Particularly, a distinct broad peak around 0.62 V in the first potassiation process without appearance in the following cycles should be related to an inevitable decomposition of electrolyte in a irreversible formation of SEI upon discharging [107]. During the discharging (potassiation) processes, the noticeable cathodic peaks at 0.97 V indicated the intercalation of K^+ into porous carbon, and sharp peaks around 0.001 V reflected a stepwise phase conversion from red P to K_xP compound, while the obvious features at 0.84 V and 1.74 V in the subsequent anodic processes should represent the corresponding reversible phase transformation during depotassiation [94]. While the overlapping positions and shapes for reversible cathodic and anodic peaks in several cycles partially testified their electrochemical reversibility during the discharging/charging processes, the change of peak intensities further pointed out the differences on the electrochemical activity and durability for various P/C composites, which were also identified by the galvanotactic discharge-charge measurements at a current density of 200 mA g^{-1} in Fig. 4(d–f). In the first cycle, the P-C-2 anode material would deliver a large discharging capacity of 1258 mA h g^{-1} and a highly reversible capacity of 739 mA h g^{-1} with an initial coulombic efficiency of 58.8%, while the P-C-1 and P-C-4 anode materials could display relatively lower discharging/charging capacities of 1073/525 and 864/502 mA h g^{-1}, signifying the key role of phosphorus loading in P/C composite. It is noteworthy that the sloping plateau below 1.0 V in the first discharging process correlated well with the irreversible cathodic peak around 0.62 V in the emergence of SEI layer. In the following cycles, a sloping region between 1.5 and 0.5 V and a reversible discharging plateau below 0.5 V separately agreed well with a repeatable cathodic peak at 0.97 V and a sharp peak around 0.001 V, while the subsequent anodic features around 0.84 and 1.74 V can be respectively observed in a highly stable charging plateau around 0.75 V and a gradually vanished stage above 1.5 V. Specifically, the P-C-2 anode material could exhibit highly stable charging capacities of 683, 635, 595, 572, 551, 520, and 512 mA h g^{-1} in the 5th, 10th, 25th, 50th, 100th, 150th, and 200th cycle, respectively. When it comes to P-C-1 anode material, the reversible capacity slowly decreased from 500 mA h g^{-1} in the 5th cycle to 400 mA h g^{-1} in the 200th cycle, while the charging capacity for P-C-4 anode material rapidly diminished to 283 mA h g^{-1} after 200 cycles. Importantly, this fast capacity decay, associated with the severe voltage hysteresis and gradual degradations of discharging/charging plateaus, should be basically ascribed to the structural incapability and instability of porous carbon in accommodating the formidable volume change of high-loading phosphorus in P/C composite upon potassiation/depotassiation. Considering the strikingly different electrochemical properties for various P/C composites with different phosphorus contents, it is still critical to balance the phosphorus loading for reversible capacity/volume variation against the

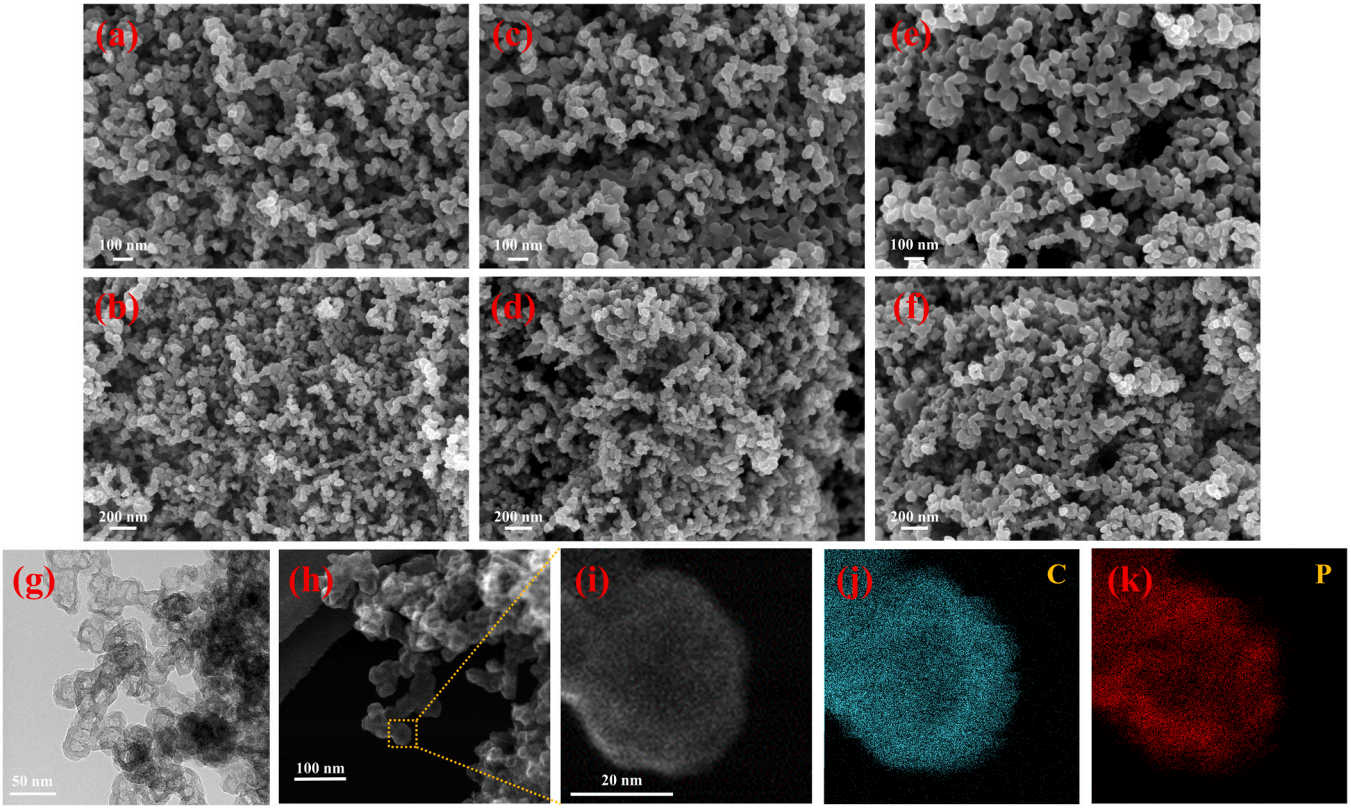

Fig. 3. Morphologies and structures for various P/C composites. SEM images for (a, b) P-C-1, (c, d) P-C-2, and (e, f) P-C-4. (g) TEM image, (h, i) STEM image, and the corresponding elemental mappings of (j) C and (k) P for P-C-2.

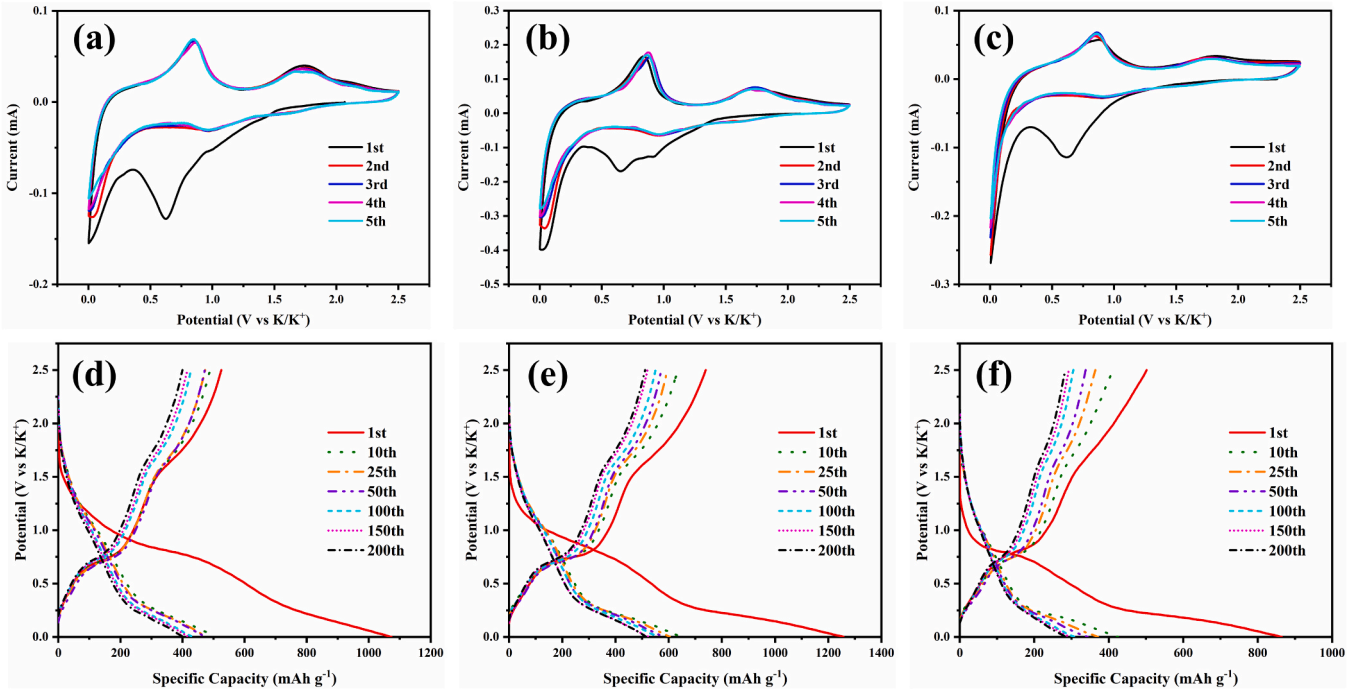

Fig. 4. Electrochemical behaviors for various P/C composites. CV curves for (a) P-C-1, (b) P-C-2, and (c) P-C-4 at a scan rate of 0.2 mV s^{-1}. Discharging and charging profiles for (d) P-C-1, (e) P-C-2, and (f) P-C-4 at a current density of 200 mA g^{-1}.

structural integrity/stability of carbon host for electrochemical reversibility/durability in the pursuit of high-energy and long-life phosphorus anode materials.

Moreover, the dramatically different electrochemical performances were also verified by cycle performances for various P/C composites. As shown in Fig. 5(a), the P-C-2 anode material would present a highest charging capacity of 512 mA h g^{-1} among various P/C composites with a 69.2% capacity retention after 200 cycles at a low current density of 200 mA g^{-1}, while the corresponding reversible capacities for P-C-1 and P-C-4 can only stabilize around 400 and 283 mA h g^{-1} with the capacity retention rates of 76.1% and 56.6%, respectively. On the one hand, a low phosphorus loading in P/C composite may partially reduce the volumetric variation degree of phosphorus upon potassiation/depotassiation, but the subsequent decrease of reversible capacity would further diminish the practical energy density of P/C anode. On the other hand, a high phosphorus content in P/C composite, accompanied by a huge volume change upon discharging/charging, could severely challenge the structural integrity/stability of P/C anode and then give rise to a rapid capacity degradation. Consequently, it is still crucial to select a desirable phosphorus loading in P/C anode material for balancing the reversible capacity against cycle life and maximizing the electrochemical reversibility/durability. Intriguingly, the similar electrochemical differences can be further seen in the comparison of cycle performances for various P/C composites at a current density of 400 mA g^{-1} (Fig. 5(b)). The P-C-2 anode material could deliver a large reversible capacity of 444 mA h g^{-1} with a 61.3% capacity retention after 500 cycles, while the P-C-1 and P-C-4 would separately display charging capacities of 333 and 194 mA h g^{-1} with capacity retention rates of 75.3% and 42.8%. When cycled at a current density of 800 mA g^{-1} over 1000 cycles in Fig. 5(c), the P-C-2 anode material would obtain a highly stable charging capacity of 368 mA h g^{-1} with a 57.7% capacity retention. Conversely, the corresponding values for P-C-1 and P-C-4 would gradually drop to 270 and 162 mA h g^{-1}, representing the capacity retention rates of 69.0% and 42.8%, respectively. Surprisingly, a highly reversible capacity of 310 mA h g^{-1} with a 55.9% capacity retention can still be achieved for P-C-2 anode materials after cycling at 1600 mA g^{-1} over 2000 cycles in Fig. 5(d). At the same time, the counterpart charging capacities for P-C-1 and P-C-4 can merely reach 211 and 129 mA h g^{-1}, corresponding to the capacity retention rates of 61.3% and 38.5%, respectively. Regardless of the relatively low initial coulombic efficiencies, the superior electrochemical stability and durability for P-C-2 anode material with an appropriate phosphorus loading should be originated from its remarkably enhanced structural integrity in stable/flexible nanostructure against large volumetric expansion/shrinkage and significantly improved electron transport/ion diffusion capabilities in conductive/porous matrix.

The outstanding rate capability and cycle stability of P-C-2 anode material were also identified in comparison of electrochemical performances for various P/C composites. As displayed in Fig. 6(a and b), the P-C-2 anode material was able to deliver large reversible capacities of 696, 630, 583, 537, and 492 mA h g^{-1} in the 5th, 15th, 25th, 35th, and 45th cycle at current densities of 100, 200, 400, 800, and 1600 mA g^{-1}, respectively. Concurrently, the P-C-1 anode material could attain reduced charging capacities of 554, 504, 478, 443, and 392 mA h g^{-1} at current densities of 100, 200, 400, 800, and 1600 mA g^{-1}, respectively. When it comes to P-C-4 anode material, the reversible capacities quickly diminished to 471, 332, 262, 225, and 191 mA h g^{-1} at current densities of 100, 200, 400, 800, and 1600 mA g^{-1}, respectively. Further increasing the current density, the P-C-2 anode material could still maintain highly stable reversible capacities of 452, 422, 391, 359, and 324 mA h g^{-1} in the 55th, 65th, 75th, 85th, and 95th cycle at current densities of 3200, 4800, 6400, 8000, and 9600 mA g^{-1}, respectively. Unfortunately, the corresponding charging capacities for P-C-1 anode material would separately decline to 331, 314, 301, 281, and 266 mA h g^{-1}, while the P-C-4 barely acquired reversible capacities of 166, 150, 125, 103, and 82 mA h g^{-1} at current densities of 3200, 4800, 6400, 8000, and 9600 mA g^{-1}, respectively. Even when the current density was increased to 11,200 mA g^{-1}, the P-C-2 anode material could still retain a highly reversible charging capacity of 287 mA h g^{-1} in the 105th cycle, which was higher than 251 mA h g^{-1} for P-C-1 and 74 mA h g^{-1} for P-C-4, hinting at a superior electrochemical adaptability of P-C-2 anode material to an extremely large current density through an unique confinement of phosphorus nanoparticles into conductive/porous carbon host with prominently enhanced electron

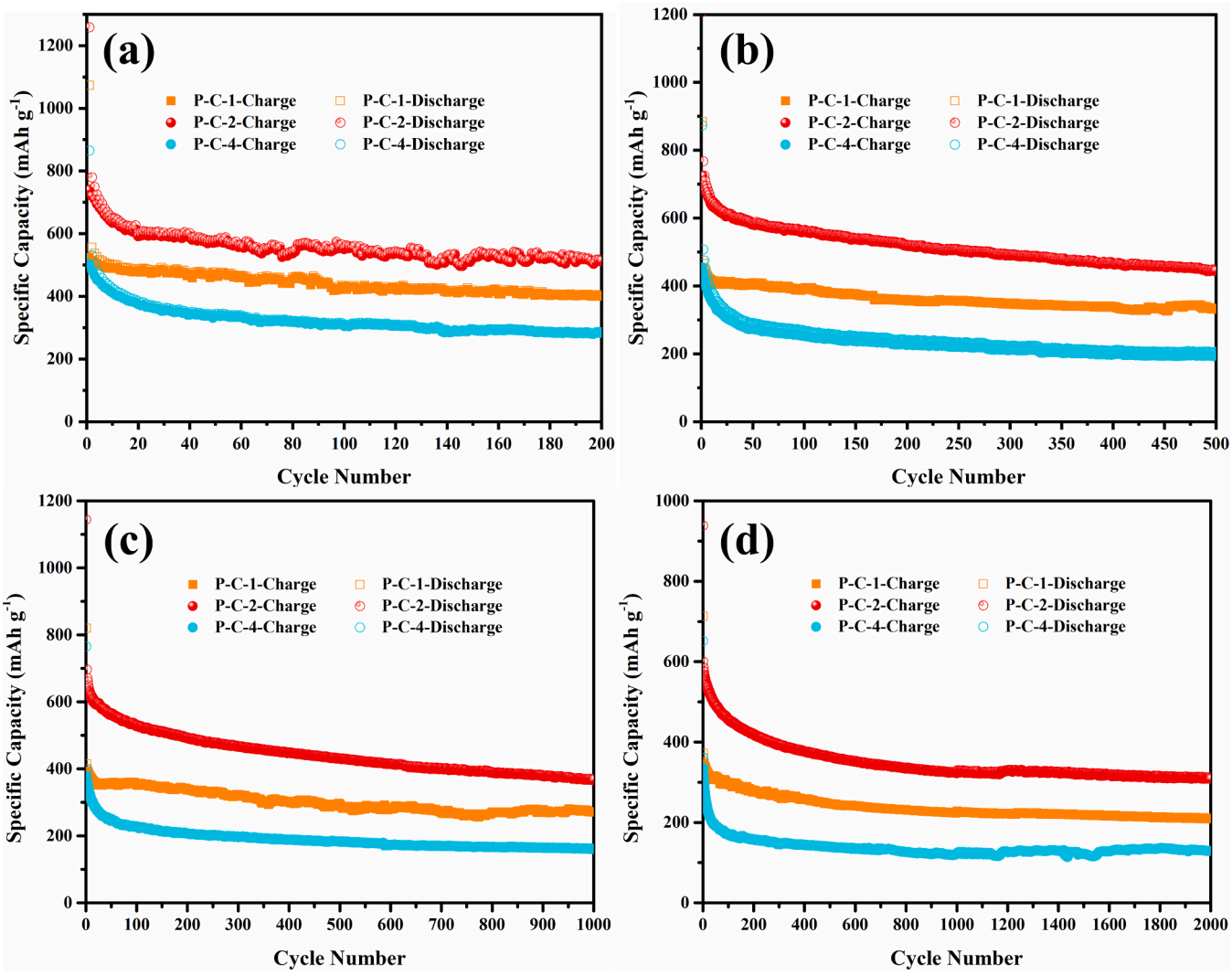

Fig. 5. Electrochemical performances for various P/C composites. Cycle performances for various P/C composites at current densities of (a) 200 mA g^{-1}, (b) 400 mA g^{-1}, (c) 800 mA g^{-1}, and (d) 1600 mA g^{-1}.

transport coefficient and ion diffusion rate. Additionally, this reversible capacity for P-C-2 anode material could gradually return back to 701 mA h g^{-1} in the 115th cycle upon cycling at 100 mA h g^{-1}, further implying its outstanding structural stability and integrity toward different volume changes at varying current densities. Even cycled at a large current density of 3200 mA g^{-1} over 10,000 cycles in Fig. 6(c), a highly reversible capacity of 212 mA h g^{-1} with a negligible 0.00597% capacity loss per cycle can still be achieved for P-C-2 anode material, while the coulombic efficiencies could immediately approach almost 100% after the gradual formation of SEI layer in the initial 20 cycles. Appealingly, an outstanding rate capability and a superior cycle stability for P-C-2 anode material have surpassed the electrochemical results in most previous reports regarding phosphorus anode materials for PIBs (Fig. S17(a and b)) [65–67,70–80,91–95,108,109], suggesting a broad application foreground of loading substantial phosphorus into various carbon hosts as highly reversible and stable anode materials for high-energy and long-life PIBs. Even among the prevailing anode materials (intercalation-type, alloy-type, and conversion-type) for PIB, this phosphorus/carbon anode materials still occupied a highly competitive position in the comparison of electrochemical performance [10,64,110–112]. Particularly, the carbon matrix in P/C composite would not only buffer the tremendous volume changes for phosphorus nanoparticles and maintain the structural integrity of anode upon continuous potassiation/depotassiation, but also facilitate the electron transport across the insulating phosphorus materials via conductive networks and ensure a rapid ion diffusion in electrode/electrolyte interface through porous nanostructure, contributing to an ultralarge reversible capacity and an ultralong cycle life with an extraordinary rate capability for P/C anode material.

In view of an exceptional electrochemical performance for P-C-2 anode material, the CV measurements were performed at scan rates of 0.2–2.0 mV s^{-1} in Fig. 7(a) to decipher the fundamental reaction kinetics and potassium storage mechanism. Critically, the charge storage of different anode materials upon potassiation/depotassiation is not only relying on the diffusion-controlled faradic reactions of K^+ intercalation/alloying/conversion from internal structure, but also dependent on the capacitance-dominated interfacial reactions of K^+ adsorption/desorption on defective surface [24–27,30,32,38,39,41,44,49,50,53,56]. Generally, the electrochemical energy can be stored in electrical double-layer capacitors (EDLCs), pseudocapacitors, and batteries, which possess quite different charge storage mechanisms [113]. Primarily, the EDLCs would perform an electrostatic accumulation of charges through reversible chemical adsorption/desorption of anions/cations and physical formation/decomposition of electrical double layer at electrode/electrolyte interface without any faradic redox reactions or phase transformations for electrodes [114]. In the view of this capacitive reaction, the capacitance for EDLCs is proportional to the specific surface area of active electrode. Conversely, the batteries would

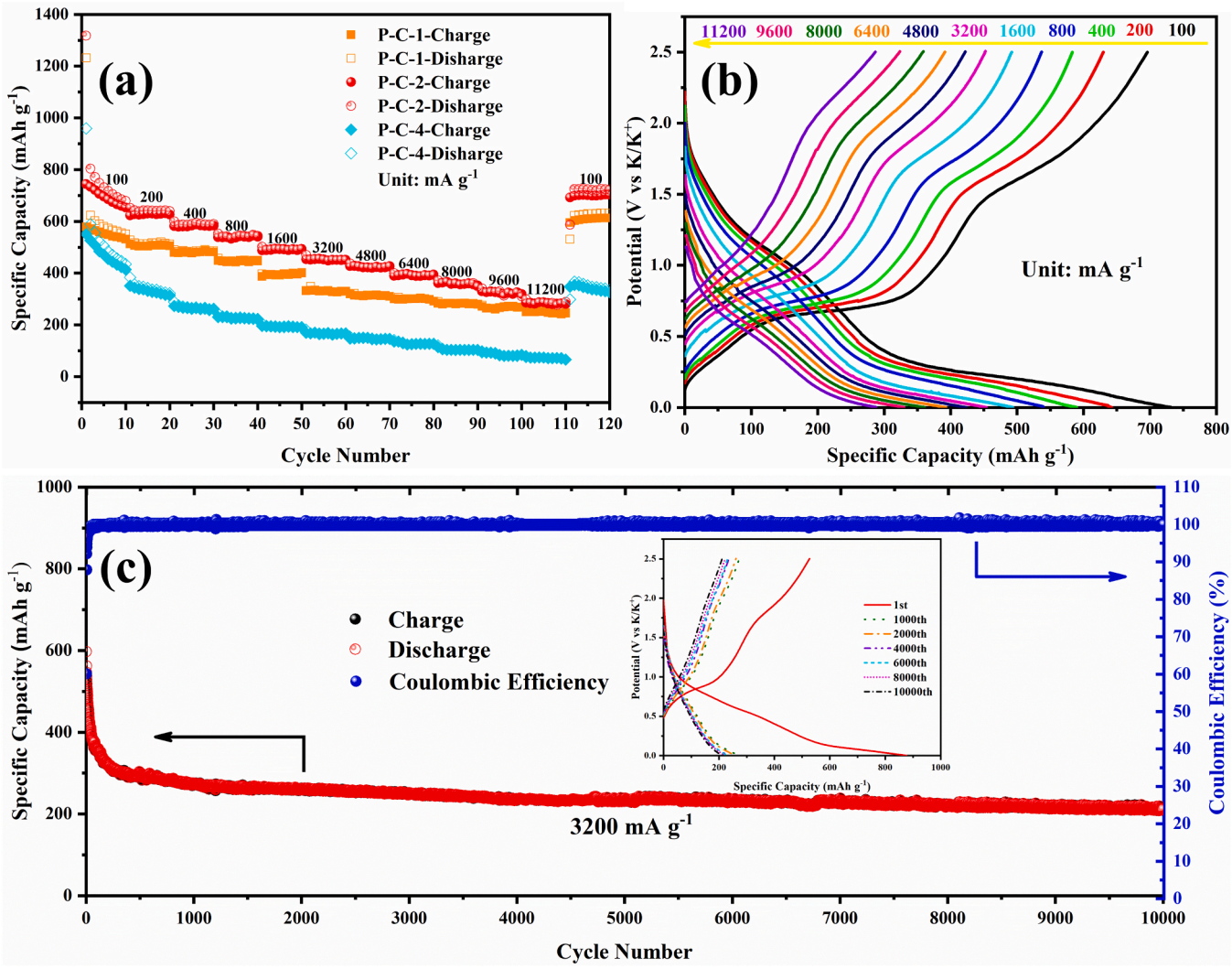

Fig. 6. Rate cycle performance for various P/C composites. (a) Rate performances for various P/C composites. (b) The corresponding discharging/charging profiles for P-C-2 at different current densities. (c) Long cycle performance for P-C-2 at a current density of 3200 mA g^{-1}, the inset is the corresponding discharging/charging profiles.

proceed a faradic redox charge storage process and a conspicuous phase transformation on electrode via intercalation/alloying/conversion reactions. Namely, the EDLCs would conduct a surface-dominated capacitive reaction with a high power density, while the batteries would carry out a solid-state diffusion-controlled redox reaction with a high energy density. Appealingly, the pseudocapacitors would balance the power density against energy density for electrochemical energy storage systems by incorporating the high-rate capacitive reactions of EDLCs with the high-capacity redox reactions of batteries [115–119]. According to classical theory from Conway [120,121], the primary pseudocapacitance can be categorized as adsorption type, redox type, and intercalation type. While the adsorption pseudocapacitance indicates a underpotential deposition of monolayer metal on the surface of other metal, the redox pseudocapacitance would reflect the electrochemical adsorption of charge carriers at or near the surface of electroactive electrodes with faradic charge transfer reactions and without any noticeable phase transformations. In terms of intercalation pseudocapacitance, the electroactive ions would intercalate into two-dimensional structures during the faradic charge storage process but without any specified phase transformations and valence state changes, which is different from the traditional intercalation reaction in batteries with clear phase transformations in faradic redox reactions. Very recently, the rational designs of nanostructure and special morphology for electrode material would further endow the faradic capacitive reactions at electrode/electrolyte interfaces, which can be called as extrinsic pseudocapacitance, while the previous three types would be intrinsic pseudocapacitance [122–124]. Even though the phosphorus anode materials are primarily supposed to proceed a multi-electron alloying reaction upon potassium storage process, it is still urgently necessary to quantitatively recognize the surface-induced capacitive contribution and further reveal the basic reaction mechanism upon potassiation/depotassiation. Hypothetically, the relationship between a specific responsive current and a corresponding scan rate generally obeys a classical power-law formula:

$$i(V) = av^b \tag{1}$$

where $i(V)$ (mA) corresponds to a specific current response at a certain voltage of V (V) and a corresponding sweep rate (mV s^{-1}), while a and b are adjustable parameters. According to a linear fitting of log ($|i(V)|$) versus log(v) plot, the accurate value of b at a fixed potential can be simply extrapolated in Fig. S18(a). Interestingly, a b value at 1.0 represents a linear relation of responsive currents with scan rates in a capacitance-dominated charge storage process, while a b value of 0.5 reflects a typical diffusion-controlled faradic redox reaction. Additionally, a b value between 0.5 and 1.0 further demonstrate the coexistence

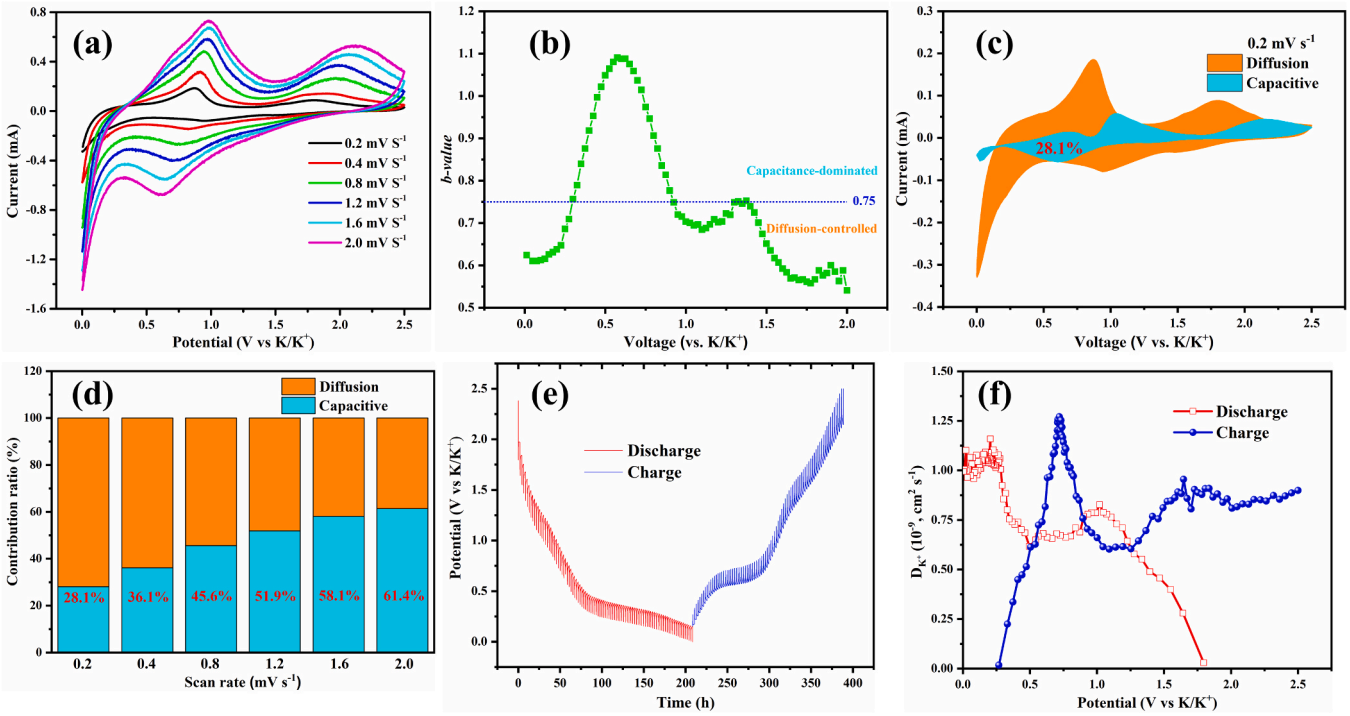

Fig. 7. Reaction mechanisms for P-C-2 anode material during the discharging/charging processes. (a) CV curves at various scan rates. (b) Calculated *b*-values plotted against the battery potentials in cathodic (potassiation) process. (c) Capacitive contribution at a scan rate of 0.2 mV s^{-1}. (d) Contribution ratios of capacitive reaction at various scan rates. (e) GITT profiles of discharging/charging processes. (f) The K^+ diffusion coefficients during discharging/charging processes.

of diffusive and capacitive behaviors in potassium storage process. In the current case, the capacitive behavior should be the surface-dominated faradic reaction in charge transfer process without any phase transformations, while the diffusive behavior should be the solid-state diffusion-controlled faradic redox reaction with noticeable phase transformations and valence state changes [115–119]. To uncover the charge storage mechanism of P-C-2 anode material, 80 values of *b* parameter at different voltages between 0.001 and 2.0 V in the discharging process were derived from Eq. (1) and further compared in Fig. 7(b). As the *b* value of 0.75 was selected as an equivalent contribution position, the diffusion-controlled redox reactions would happen at the beginning of potassiation between 2.0 and 1.35 V for K^+ intercalation into carbon and reappear at the deep discharging process between 0.3 and 0.001 V for K^+ alloying with phosphorus, while the capacitance-dominated interfacial reactions could prefer to occur in the middle of potassiation between 1.35 and 0.3 V. Even though the increase of sweep rate partially changed the voltage positions of cathodic and anodic peaks by electrochemical polarization, the retention of these features further validates the steady reaction kinetics and excellent rate capability for this P/C anode material. Based on the well-established relationship between responsive current and scan rate in Eq. (1), the diffusive and capacitive contributions can be further quantified in the following equation:

$$i(V) = k_1 v + k_2 v^{1/2} \tag{2}$$

where the k_1v with a *b* value of 1.0 indicates a surface-dominated capacitive contribution and $k_2v^{1/2}$ with a *b* value of 0.5 demonstrates a solid-state diffusive contribution in a certain current response at a specific voltage. With the assistance of a linear fitting for $i(V)/v^{1/2}$ versus $v^{1/2}$ profile at a fixed voltage for different scan rates, the corresponding value of k_1 could be facilely obtained. Upon plotting different k_1v results against various potentials at a specific scan rate of *v*, the capacitive contribution to responsive current can be instantly achieved. As identified in Fig. 7(c), the P-C-2 anode material would possess a considerable contribution of 28.1% from surface-induced capacitive reactions to charge storage process at a low scan rate of 0.2 mV s^{-1}, while the emerging regions for pseudocapacitive behaviors correspond well with the evolution of *b* values. Appealingly, the surface-induced capacitive contribution to potassium storage in Fig. 7(d) would strikingly increase to 36.1%, 45.6%, 51.9%, and 58.1% at scan rates of 0.4, 0.8, 1.2, and 1.6 mV s^{-1} in Fig. S18(b–f), respectively. Upon further increasing the scan rate to 2.0 mV s^{-1}, this key parameter could surprisingly reach a high value of 61.4%, hinting at a remarkable electrochemical contribution from surface-dominated capacitive reactions to charge storage process to an outstanding rate capability and a superior cycle stability for P-C-2 anode material. To further elucidate the reaction kinetics for P-C-2 anode material upon potassiation/depotassiation, the GITT measurements as depicted in Fig. 7(e) were applied to derive the K^+ diffusion coefficients during the discharging/charging processes from the following equation in Fick's second law [26,38,39,44]:

$$D = \frac{4}{\pi\tau}\left(\frac{m_B V_m}{M_B S}\right)^2 \left(\frac{\Delta E_s}{\Delta E_\tau}\right)^2, \quad \tau \ll \frac{L^2}{D_{K^+}} \tag{3}$$

where τ is a galvanostatic current pulse time (s), while m_B, V_m, and M_B are actual mass, molar volume, and molar mass of active material, respectively. Moreover, *S* and *L* are surface area and thickness for electrode. Importantly, ΔE_s represents a voltage change of electrode at a steady state after the intermittent galvanostatic discharging/charging, while ΔE_τ reflects a voltage change of electrode at a dynamic state upon applying the galvanostatic discharging/charging current. In this case, the galvanostatic current pulse time and steady state period were set as 10 min and 2 h at a current density of 50 mA g^{-1}, respectively. As the weight of active material and surface area of electrode can be easily accessed in the electrochemical experiments, the value of V_m/M_B could be further obtained from the density of active material, yielding a calculated K^+ diffusion coefficient at a certain potential. When plotted various K^+ diffusion coefficients as a function of the corresponding potentials in Fig. 7(f), the changes of reaction kinetics upon potassiation/depotassiation can be visualized. Attractively, the K^+ diffusion coefficient would continue to increase at the beginning of potassiation and

then reach a moderate value of 0.83×10^{-9} cm^2 s^{-1} at 1.0 V. After a gradual drop to $\sim 0.61 \times 10^{-9}$ cm^2 s^{-1} at 0.5 V, this parameter would apparently increase to 1.15×10^{-9} cm^2 s^{-1} at 0.2 V and maintain a high value at the deep discharging state, implying a superior kinetic behavior of solid-state diffusion-controlled redox reactions for P-C-2 anode material. In terms of charging process, the K^+ diffusion coefficient would rapidly increase to 1.27×10^{-9} cm^2 s^{-1} at 0.72 V, then gradually decrease to 0.60×10^{-9} cm^2 s^{-1} at 1.25 V, and finally reach 0.95×10^{-9} cm^2 s^{-1} at 1.65 V, hinting at an outstanding K^+ diffusion capability upon the depotassiation process. Overall, the effective confinement of phosphorus nanoparticles into porous and conductive carbon host could not only significantly promote the electrochemical contribution from surface-dominated capacitive reactions to charge storage process, but also remarkably boost the K^+ diffusion capability across the solid-state electrode material and dramatically accelerate the diffusion-controlled redox reactions upon potassiation/depotassiation, further boosting the electrochemical reversibility and durability at high rates for P-C-2 anode material.

In addition, the structural evolution of P/C electrode upon cycling was further observed in Fig. 8(a–d). Compared with the fresh electrode presenting a uniform distribution of P/C nanoparticles in Fig. 8(a), the cycled electrodes could basically retain the pristine nanostructure of P/C composites in Fig. 8(b–d), while the electrically insulating SEI layer would continue to grow on the surface of active material and stabilize the structure of P/C nanoparticles upon repeated potassiation/depotassiation. When it comes to the discharged P/C electrode, the corresponding XRD pattern in Fig. 8(e) would exhibit three obvious peaks at 29.5°, 31.0°, and 35.2°, which can be separately assigned to (130), (114), and (200) planes for K_4P_3 (JCPDS No. 01-079-0033). As the first charge capacity for porous carbon could reach 150 mA h g^{-1} at a current density of 100 mA g^{-1} in Fig. S16, an initial reversible capacity of 744 mA h g_{p+c}^{-1} for P-C-2 anode material with a 59.4 wt% phosphorus loading should correspond to a large reversible capacity of 1150 mA h g_p^{-1} for phosphorus, which is approaching a theoretical specific capacity of 1154 mA h g^{-1} for phosphorus in the emergence of K_4P_3 upon potassiation. Consequently, the phase identification on the discharged products of P-C-2 anode material agrees well with its electrochemical properties. Unfortunately, the reaction mechanisms of phosphorus anode materials in PIBs are still ambiguous in previous reports, while the formation of discharged product upon potassiation is also unclear. In the early studies, the KP was found as a major discharged product for black P in graphite [67] and red P on 3D carbon nanosheet

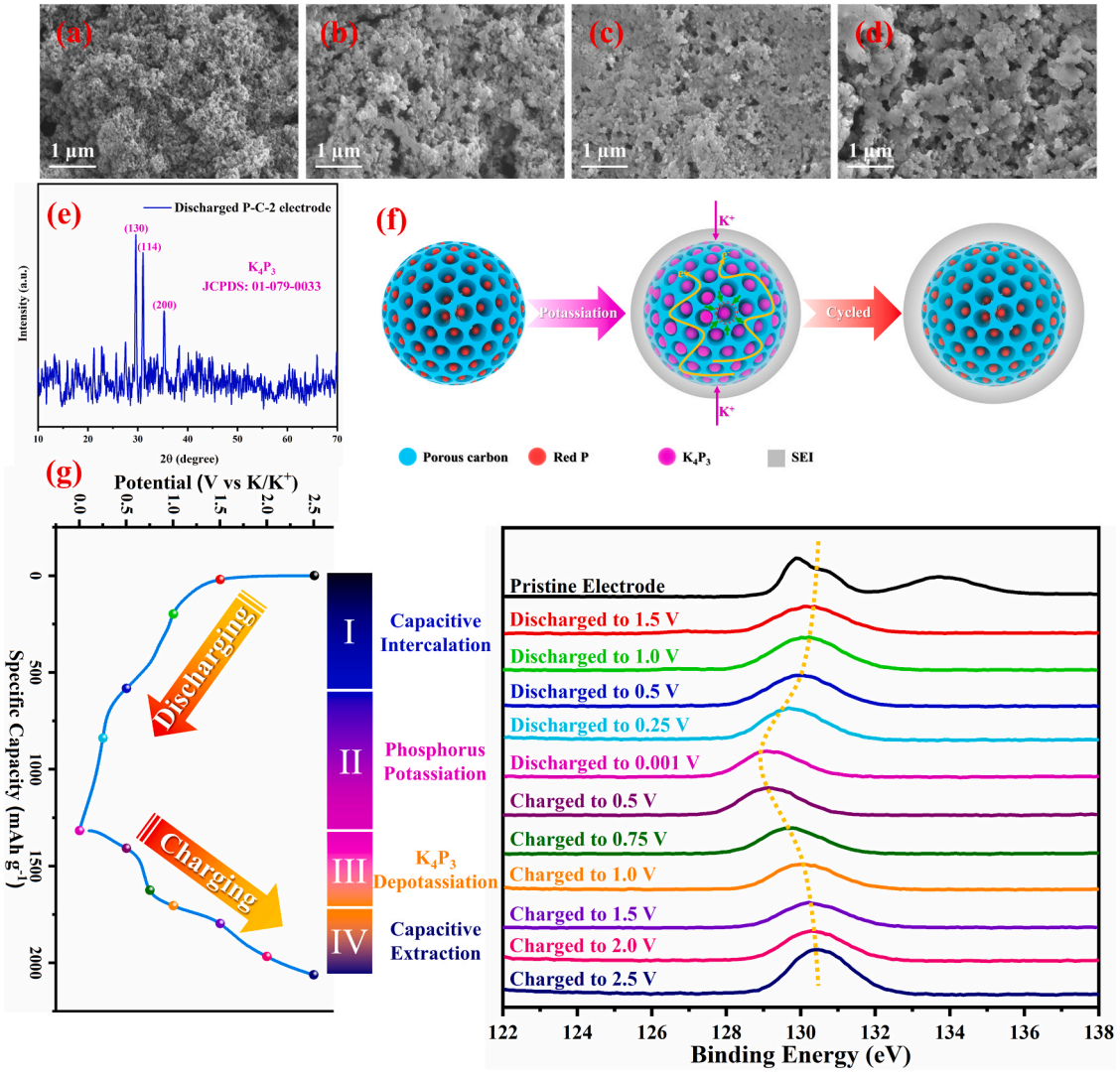

Fig. 8. Structural evolution and phase transformation of P-C-2 anode material upon potassiation/depotassiation. SEM images for (a) pristine P-C-2 electrode and electrodes after (b) 10 cycles, (c) 25 cycles, and (d) 50 cycles at a current density of 200 mA g^{-1}. (e) XRD pattern for discharged P-C-2 electrode. (f) Structural evolution of P-C-2 anode material upon potassiation and cycling. (g) *Ex-situ* P 2p X-ray photoemission spectroscopies (in right position) for P-C-2 electrodes at different states (in left position) during the discharging/charging processes with a current density of 100 mA g^{-1}.

[93], accompanying by the relatively low reversible capacities. Later, different research groups reported K_4P_3 as a new discharged product for red P in hollow carbon nanofibers [94] and rGO coated phosphorene [125]. Very recently, Chen and colleagues proposed a reaction route of phosphorus upon potassiation, involving a stepwise transformation from red P to KP_{15}, K_3P_{11}, K_4P_6, KP, and K_4P_3, respectively [95]. However, these results have been derived from *ex-situ* measurements, especially *ex-situ* XRD, which might not be able to capture the air-sensitive and unstable intermediates and products. Intriguingly, Zaiping Guo's group conducted a series of *in-operando* synchrotron XRD characterizations for different phosphides (GeP_5 [76] and Sn_4P_3 [78]) and observed an emergence of K_3P as discharged product upon potassiation, which corresponded well with their initial discovery on the formation of discharged product for Sn_4P_3 by *ex-situ* XRD [65]. Additionally, the same conclusion on the formation of K_3P as discharged product has also been reached by *ex-situ* observations of potassiation for SnP_3 [79], Sn_4P_3 [77], Se_3P_4 [81], and $Bi_{0.5}Sb_{0.5}$@P [126]. Generally, the *ex-situ* characterization of discharged product strictly required a complicated and difficult procedure, involving an initial electrochemical test of coin cells, a subsequent disassembly of coin-cells in Ar-filled glove box, a collection of air-sensitive discharged electrode powder, and a careful characterization of unstable discharged product by XRD. As the gradual changes of crystalline phases and physicochemical properties for these metastable discharged products would remarkably affect the characterization results and experimental conclusions, it is still urgently needed to proceed *in-situ* or *in-operando* X-ray characterizations on red P upon potassiation/depotassiation for revealing the underlying phase transformation and reaction mechanism. Fig. 8(f) further illustrates the structural evolution of P-C-2 anode material upon potassiation and cycling. Appealingly, the highly stable and porous carbon host, which efficiently encapsulate phosphorus nanoparticles into large-volume mesopores, could not only endow abundant electron transport channels in conductive networks for insulating phosphorus and facilitate K^+ diffusion across the electrolyte/electrode interface through a rapid electrolyte permeation in porous nanostructure, but also cushion the huge volume expansion/shrinkage for phosphorus nanoparticles upon potassiation/depotassiation and further maintain the structural integrity of P/C composite upon cycling. At the same time, the gradually accumulated SEI layer on the surface of active material would also play a vital role in anchoring the P/C nanoparticles to conductive agent and polymer binder without losing electrical contact to current collector. To understand the reaction mechanism involving phase transformation and structure evolution for phosphorus anode upon potassiation/depotassiation processes, the *ex-situ* P 2p X-ray photoemission spectroscopies were conducted for P-C-2 anode material during the discharging and charging processes, as shown in Fig. 8(g). Similarly, the pristine electrode would display the typical P $2p_{2/3}$ and P $2p_{1/3}$ features for P–P bonding around 130.5 eV and a broad character at 133.8 eV for P–O bonding, which are consistent with XPS result in Fig. 2(d) for P-C-2 anode material. When discharged to 1.5 V, the electrode would exhibit a merged broad peak around 130.2 eV, while the previous feature for P–O bonding at high energy region completely disappeared. During the discharging period at 1.5–0.5 V, the remaining broad peak would mildly shift to low-energy region, signifying a predominated but efficient diffusion of K^+ across the porous carbon nanostructure without an effective alloying reaction for phosphorus. In a deep discharging process (< 0.5 V), this broad character could distinctly move to 129.7 eV at 0.25 V and 129.1 eV at 0.001 V, demonstrating an apparent electrochemical reduction of phosphorus in the emergence of K_4P_3 during a sluggish alloying reaction with K^+. Specifically, a complete disappearance of P-O character at high energy position during the discharging process clearly manifests a greatly suppressed parasitic reaction between active phosphorus and reactive electrolyte via a highly robust and conductive carbon matrix. When it comes to charging process, the position for previous broad peak barely changes at 0.5 V, but remarkably shifts to 129.7 eV at 0.75 V and 130.1 eV at 1.0 V, verifying an effective depotassiation of K_4P_3 and a reversible formation of phosphorus. At the end of charging process, this broad feature would gradually return back to its pristine position around 130.5 eV at 2.5 V, further identifying a superior electrochemical reversibility for P-C-2 anode material. Critically, the phosphorus anode would prefer to proceed a potassiation reaction below 0.5 V in the discharging process and a depotassiation reaction at 0.5–1.0 V in the charging process. Based on the electrochemical and spectroscopic characterizations in Figs. 7(a–d) and 8(g), the P-C-2 anode would proceed an initial capacitive K^+ intercalation into the porous/conductive carbon matrix (> 0.5 V) with a subsequent potassiation of phosphorus nanoparticles (< 0.5 V) during the discharging process and conduct a noticeable depotassiation of K_4P_3 products (< 1.0 V) with a following capacitive K^+ extraction from the robust carbon nanostructure (> 1.0 V) during the charging process. It is worth emphasizing that the rational and efficient confinement of phosphorus nanoparticles into porous carbon materials would not only ameliorate the structural integrity/stability of phosphorus upon huge volume expansion/shrinkage and provide abundant electron/ion migration channels via a highly robust/conductive carbon matrix, but also incorporate the surface-induced capacitive reactions in carbon nanostructure with diffusion-controlled alloying/dealloying reactions and further contribute to the charge storage process during discharging/charging processes.

Admittedly, the utilization of porous carbon nanomaterial with a large surface area and a huge pore volume would trigger its severe parasitic reaction with reactive electrolyte in the emergence of SEI layer and further diminish the corresponding coulombic efficiency, but the robust and conductive nanostructure/framework could primarily offer abundant channels for K^+ diffusion/electron transport toward the electronically/ionically insulating phosphorus, remarkably cushion the huge volume expansion/shrinkage of phosphorus upon potassiation/depotassiation, and further boost the electrochemical reversibility/durability of phosphorus/carbon anode during cycling. Concurrently, the rational nanoconfinement of phosphorus into porous carbon would notably downsize the phosphorus from micrometer to nanometer, apparently shorten the K^+/electron migration pathways, effectively guarantee a sufficient contact of phosphorus to electrolyte, and further maximize the electrochemical activity of phosphorus anode material. However, it is still urgent to address this challenge of poor coulombic efficiency for phosphorus/carbon anode material in the commercialization of potassium-ion batteries. Our group has been working on the surface modifications of phosphorus/carbon anodes via atomic layer deposition (ALD) and molecular layer deposition (MLD) with thickness/composition controllability and coating uniformity/conformity to suppress their side reactions with reactive electrolyte and maintain the structural stability against large volume variation [127–130].

4. Conclusion

In summary, the phosphorus nanoparticles were rationally confined into a commercially available porous carbon. Benefitted from an improved structural integrity with abundant electronic/ionic migration pathways for electrically/ionically insulating phosphorus in a highly porous/conductive/robust carbon matrix upon potassiation/depotassiation, the P-C-2 electrode with a desirable phosphorus content of 59.4 wt% could deliver a large initial charging capacity of 744 mA h g^{-1} at a current density of 100 mA g^{-1}, a highly reversible capacity of 212 mA h g^{-1} at 3200 mA g^{-1} over 10,000 cycles, an outstanding rate capability of 287 mA h g^{-1} at 11,200 mA g^{-1}. According to various electrochemical and spectroscopic characterizations, the capacitive intercalation/extraction of K^+ in carbon nanostructure at a relatively high voltage would efficiently facilitate the electron transport/ion diffusion processes and significantly contribute to the charge storage process during cycling. Furthermore, the phosphorus nanomaterials would tend to proceed an effective potassiation below 0.5 V upon discharging and a subsequent depotassiation below 1.0 V upon charging,

accompanied by a reversible formation and decomposition of K_4P_3 as a discharged product. This novel research on designing high-performance phosphorus anodes and revealing the fundamental reaction mechanisms would throw lights on the development of practical PIBs with a low manufacturing cost, a high energy density, a long cycle life, and a reliable working capability.

CRediT authorship contribution statement

Wei Xiao: Conceptualization, Data curation, Formal analysis, Funding acquisition, Methodology, Investigation, Writing–original draft. **Xifei Li**: Funding acquisition, Project administration, Writing – review & editing. **Bin Cao**: Methodology, Investigation. **Gang Huang**: Methodology, Investigation. **Chong Xie**: Methodology, Investigation. **Jian Qin**: Methodology, Investigation. **Huijuan Yang**: Methodology. **Jingjing Wang:** Methodology. **Xueliang Sun**: Project administration, Writing – review & editing. All authors discussed the experimental results and proofed the final manuscript.

Declaration of Competing Interest

The authors declare that they have no known competing financial interests or personal relationships that could have appeared to influence the work reported in this paper.

Acknowledgments

This research was supported by the National Natural Science Foundation of China (51672189, 51902251, 51801153, 51802261, and 52072298), China Postdoctoral Science Foundation (2018M643697, 2019T120930, and 2019M653705), Natural Science Foundation of Shaanxi Province (2019JQ-748, 2020JQ-638 and 2020JC-41), Joint Foundation in Natural Science Basic Research Plan of Shaanxi Province (2019JLP-04), and Xi'an Science and Technology Project of China (201805037YD15CG21(20)). The authors are grateful to the technical assistance from Xiaoqin Wen in Shiyanjia Lab (www.shiyanjia.com) for XPS analysis.

Appendix A. Supporting information

Supplementary data associated with this article can be found in the online version at doi:10.1016/j.nanoen.2021.105772.

References

[1] J.-M. Tarascon, M. Armand, Issues and challenges facing rechargeable lithium batteries, Nature 414 (2001) 359–367.
[2] M. Armand, J.-M. Tarascon, Building better batteries, Nature 451 (2008) 652–657.
[3] D. Larcher, J.-M. Tarascon, Towards greener and more sustainable batteries for electrical energy storage, Nat. Chem. 7 (2015) 19–29.
[4] N. Yabuuchi, K. Kubota, M. Dahbi, S. Komaba, Research development on sodium-ion batteries, Chem. Rev. 114 (2014) 11636–11682.
[5] X. Wu, D.P. Leonard, X. Ji, Emerging non-aqueous potassium-ion batteries: challenges and opportunities, Chem. Mater. 29 (2017) 5031–5042.
[6] J. Zhang, T. Liu, X. Cheng, M. Xia, R. Zheng, N. Peng, H. Yu, M. Shui, J. Shu, Development status and future prospect of non-aqueous potassium ion batteries for large scale energy storage, Nano Energy 60 (2019) 340–361.
[7] W. Zhang, Y. Liu, Z. Guo, Approaching high-performance potassium-ion batteries via advanced design strategies and engineering, Sci. Adv. 5 (2019), eaav7412.
[8] J.C. Pramudita, D. Sehrawat, D. Goonetilleke, N. Sharma, An initial review of the status of electrode materials for potassium-ion batteries, Adv. Energy Mater. 7 (2017), 1602911.
[9] H. Kim, J.C. Kim, M. Bianchini, D.-H. Seo, J. Rodriguez-Garcia, G. Ceder, Recent progress and perspective in electrode materials for K-ion batteries, Adv. Energy Mater. 8 (2018), 1702384.
[10] T. Hosaka, K. Kubota, A.S. Hameed, S. Komaba, Research development on K-ion batteries, Chem. Rev. 120 (2020) 6358–6466.
[11] Y. Mizutani, T. Abe, K. Ikeda, E. Ihara, M. Asano, T. Harada, M. Inaba, Z. Ogumi, Graphite intercalation compounds prepared in solutions of alkali metals in 2-methyltetrahydrofuran and 2,5-dimethyltetrahydrofuran, Carbon 35 (1997) 61–65.
[12] Y. Mizutani, T. Abe, M. Inaba, Z. Ogumi, Creation of nanospaces by intercalation of alkali metals into graphite in organic solutions, Synth. Met. 125 (2001) 153–159.
[13] Z. Jian, W. Luo, X. Ji, Carbon electrodes for K-ion batteries, J. Am. Chem. Soc. 137 (2015) 11566–11569.
[14] S. Komaba, T. Hasegawa, M. Dahbi, K. Kubota, Potassium intercalation into graphite to realize high-voltage/high-power potassium-ion batteries and potassium-ion capacitors, Electrochem. Commun. 60 (2015) 172–175.
[15] Z. Xing, Y. Qi, Z. Jian, X. Ji, Polynanocrystalline graphite: a new carbon anode with superior cycling performance for K-ion batteries, ACS Appl. Mater. Interfaces 9 (2017) 4343–4351.
[16] B. Cao, Q. Zhang, H. Liu, B. Xu, S. Zhang, T. Zhou, J. Mao, W.K. Pang, Z. Guo, A. Li, J. Zhou, X. Chen, H. Song, Graphitic carbon nanocage as a stable and high power anode for potassium-ion batteries, Adv. Energy Mater. 8 (2018), 1801149.
[17] Z. Jian, Z. Xing, C. Bommier, Z. Li, X. Ji, Hard carbon microspheres: potassium-ion anode versus sodium-ion anode, Adv. Energy Mater. 6 (2016), 1501874.
[18] W. Wang, J. Zhou, Z. Wang, L. Zhao, P. Li, Y. Yang, C. Yang, H. Huang, S. Guo, Short-range order in mesoporous carbon boosts potassium-ion battery performance, Adv. Energy Mater. 8 (2018), 1701648.
[19] Y. Liu, Y.X. Lu, Y.S. Xu, Q.S. Meng, J.C. Gao, Y.G. Sun, Y.S. Hu, B.B. Chang, C. T. Liu, A.M. Cao, Pitch-derived soft carbon as stable anode material for potassium ion batteries, Adv. Mater. 32 (2020), 2000505.
[20] Z. Jian, S. Hwang, Z. Li, A.S. Hernandez, X. Wang, Z. Xing, D. Su, X. Ji, Hard-soft composite carbon as a long-cycling and high-rate anode for potassium-ion batteries, Adv. Funct. Mater. 27 (2017), 1700324.
[21] D. Li, X. Ren, Q. Ai, Q. Sun, L. Zhu, Y. Liu, Z. Liang, R. Peng, P. Si, J. Lou, J. Feng, L. Ci, Facile fabrication of nitrogen-doped porous carbon as superior anode material for potassium-ion batteries, Adv. Energy Mater. 8 (2018), 1802386.
[22] J. Yang, Z. Ju, Y. Jiang, Z. Xing, B. Xi, J. Feng, S. Xiong, Enhanced capacity and rate capability of nitrogen/oxygen dual-doped hard carbon in capacitive potassium-ion storage, Adv. Mater. 30 (2018), 1700104.
[23] M. Chen, W. Wang, X. Liang, S. Gong, J. Liu, Q. Wang, S. Guo, H. Yang, Sulfur/oxygen codoped porous hard carbon microspheres for high-performance potassium-ion batteries, Adv. Energy Mater. 8 (2018), 1800171.
[24] J. Ruan, Y. Zhao, S. Luo, T. Yuan, J. Yang, D. Sun, S. Zheng, Fast and stable potassium-ion storage achieved by in situ molecular self-assembling N/O dual-doped carbon network, Energy Storage Mater. 23 (2019) 46–54.
[25] X. Chang, X. Zhou, X. Ou, C.S. Lee, J. Zhou, Y. Tang, Ultrahigh nitrogen doping of carbon nanosheets for high capacity and long cycling potassium ion storage, Adv. Energy Mater. 9 (2019), 1902672.
[26] Y. Liu, H. Dai, L. Wu, W. Zhou, L. He, W. Wang, W. Yan, Q. Huang, L. Fu, Y. Wu, A large scalable and low-cost sulfur/nitrogen dual-doped hard carbon as the negative electrode material for high-performance potassium-ion batteries, Adv. Energy Mater. 9 (2019), 1901379.
[27] J. Lu, C. Wang, H. Yu, S. Gong, G. Xia, P. Jiang, P. Xu, K. Yang, Q. Chen, Oxygen/fluorine dual-doped porous carbon nanopolyhedra enabled ultrafast and highly stable potassium storage, Adv. Funct. Mater. 29 (2019), 1906126.
[28] D.-S. Bin, X.-J. Lin, Y.-G. Sun, Y.-S. Xu, K. Zhang, A.-M. Cao, L.-J. Wan, Engineering hollow carbon architecture for high-performance K-ion battery anode, J. Am. Chem. Soc. 140 (2018) 7127–7134.
[29] Y. Wang, Z. Wang, Y. Chen, H. Zhang, M. Yousaf, H. Wu, M. Zou, A. Cao, R.P. S. Han, Hyperporous sponge interconnected by hierarchical carbon nanotubes as a high-performance potassium-ion battery anode, Adv. Mater. 30 (2018), 1802074.
[30] X. Zhou, L. Chen, W. Zhang, J. Wang, Z. Liu, S. Zeng, R. Xu, Y. Wu, S. Ye, Y. Feng, X. Cheng, Z. Peng, X. Li, Y. Yu, Three-dimensional ordered macroporous metal–organic framework single crystal-derived nitrogen-doped hierarchical porous carbon for high-performance potassium-ion batteries, Nano Lett. 19 (2019) 4965–4973.
[31] J. Han, C. Zhang, D. Kong, X. He, J. Xiao, F. Chen, Y. Tao, Y. Wan, Q.-H. Yang, Flowable sulfur template induced fully interconnected pore structures in graphene artefacts towards high volumetric potassium storage, Nano Energy 72 (2020), 104729.
[32] W. Zhang, J. Ming, W. Zhao, X. Dong, M.N. Hedhili, P.M.F.J. Costa, H. N. Alshareef, Graphitic nanocarbon with engineered defects for high-performance potassium-ion battery anodes, Adv. Funct. Mater. 29 (2019), 1903641.
[35] V. Lakshmi, Y. Chen, A.A. Mikhaylov, A.G. Medvedev, I. Sultana, M.M. Rahman, O. Lev, P.V. Prikhodchenko, A.M. Glushenkov, Nanocrystalline SnS_2 coated onto reduced graphene oxide: demonstrating the feasibility of a non-graphitic anode with sulfide chemistry for potassium-ion batteries, Chem. Commun. 53 (2017) 8272–8275.
[36] K. Huang, Z. Xing, L. Wang, X. Wu, W. Zhao, X. Qi, H. Wang, Z. Ju, Direct synthesis of 3D hierarchically porous carbon/Sn composites via in situ generated NaCl crystals as templates for potassium-ion batteries anode, J. Mater. Chem. A 6 (2018) 434–442.
[37] D.-S. Bin, S.-Y. Duan, X.-J. Lin, L. Liu, Y. Liu, Y.-S. Xu, Y.-G. Sun, X.-S. Tao, A.-M. Cao, L.-J. Wan, Structural engineering of SnS_2/graphene nanocomposite for high-performance K-ion battery anode, Nano Energy 60 (2019) 912–918.
[38] X. Ge, S. Liu, M. Qiao, Y. Du, Y. Li, J. Bao, X. Zhou, Enabling superior electrochemical properties for highly efficient potassium storage by impregnating ultrafine Sb nanocrystals within nanochannel-containing carbon nanofibers, Angew. Chem. Int. Ed. 58 (2019) 14578–14583.
[39] J. Li, N. Zhuang, J. Xie, X. Li, W. Zhuo, H. Wang, J.B. Na, X. Li, Y. Yamauchi, W. Mai, K-ion storage enhancement in Sb_2O_3/reduced graphene oxide using ether-based electrolyte, Adv. Energy Mater. 10 (2020), 1903455.

[40] B. Wang, Z. Deng, Y. Xia, J. Hu, H. Li, H. Wu, Q. Zhang, Y. Zhang, H. Liu, S. Dou, Realizing reversible conversion-alloying of Sb(V) in polyantimonic acid for fast and durable lithium- and potassium-ion storage, Adv. Energy Mater. 10 (2020), 1903119.

[41] Z. Wu, G. Liang, W.K. Pang, T. Zhou, Z. Cheng, W. Zhang, Y. Liu, B. Johannessen, Z. Guo, Coupling topological insulator $SnSb_2Te_4$ nanodots with highly doped graphene for high-rate energy storage, Adv. Mater. 32 (2020), 1905632.

[42] K. Lei, C. Wang, L. Liu, Y. Luo, C. Mu, F. Li, J. Chen, A porous network of bismuth used as the anode material for high-energy-density potassium-ion batteries, Angew. Chem. Int. Ed. 57 (2018) 4687–4691.

[43] Q. Zhang, J. Mao, W.K. Pang, T. Zheng, V. Sencadas, Y. Chen, Y. Liu, Z. Guo, Boosting the potassium storage performance of alloy-based anode materials via electrolyte salt chemistry, Adv. Energy Mater. 8 (2018), 1703288.

[44] H. Yang, R. Xu, Y. Yao, S. Ye, X. Zhou, Y. Yu, Multicore–shell Bi@N-doped carbon nanospheres for high power density and long cycle life sodium- and potassium-ion anodes, Adv. Funct. Mater. 29 (2019), 1809195.

[45] T. Jin, H. Li, Y. Li, L. Jiao, J. Chen, Intercalation pseudocapacitance in flexible and self-standing V_2O_3 porous nanofibers for high-rate and ultra-stable K ion storage, Nano Energy 50 (2018) 462–467.

[46] Y. Liu, D. He, Q. Tan, Q. Wan, K. Han, Z. Liu, P. Li, F. An, X. Qu, A synergetic strategy for an advanced electrode with Fe_3O_4 embedded in a 3D N-doped porous graphene framework and a strong adhesive binder for lithium/potassium ion batteries with an ultralong cycle lifespan, J. Mater. Chem. A 7 (2019) 19430–19441.

[47] D. Adekoya, H. Chen, H.Y. Hoh, T. Gould, M.-S.J.T. Balogun, C. Lai, H. Zhao, S. Zhang, Hierarchical Co_3O_4@N-doped carbon composite as an advanced anode material for ultrastable potassium storage, ACS Nano 14 (2020) 5027–5035.

[48] M. Mao, C. Cui, M. Wu, M. Zhang, T. Gao, X. Fan, J. Chen, T. Wang, J. Ma, C. Wang, Flexible ReS_2 nanosheets/N-doped carbon nanofibers-based paper as a universal anode for alkali (Li, Na, K) ion battery, Nano Energy 45 (2018) 346–352.

[49] Y. Zhao, J. Zhu, S.J.H. Ong, Q. Yao, X. Shi, K. Hou, Z.J. Xu, L. Guan, High-rate and ultralong cycle-life potassium ion batteries enabled by in situ engineering of yolk-shell FeS_2@C structure on graphene matrix, Adv. Energy Mater. 8 (2018), 1802565.

[50] J. Chu, W.A. Wang, J. Feng, C.-Y. Lao, K. Xi, L. Xing, K. Han, Q. Li, L. Song, P. Li, X. Li, Y. Bao, Deeply nesting zinc sulfide dendrites in tertiary hierarchical structure for potassium ion batteries: enhanced conductivity from interior to exterior, ACS Nano 13 (2019) 6906–6916.

[51] L. Yang, W. Hong, Y. Zhang, Y. Tian, X. Gao, Y. Zhu, G. Zou, H. Hou, X. Ji, Hierarchical NiS_2 modified with bifunctional carbon for enhanced potassium-ion storage, Adv. Funct. Mater. 29 (2019), 1903454.

[52] J. Ge, L. Fan, J. Wang, Q. Zhang, Z. Liu, E. Zhang, Q. Liu, X. Yu, B. Lu, $MoSe_2$/N-doped carbon as anodes for potassium-ion batteries, Adv. Energy Mater. 8 (2018), 1801477.

[53] H. Huang, J. Cui, G. Liu, R. Bi, L. Zhang, Carbon-coated $MoSe_2$/MXene hybrid nanosheets for superior potassium storage, ACS Nano 13 (2019) 3448–3456.

[54] C.A. Etogo, H. Huang, H. Hong, G. Liu, L. Zhang, Metal–organic-frameworks-engaged formation of $Co_{0.85}Se$@C nanoboxes embedded in carbon nanofibers film for enhanced potassium-ion storage, Energy Storage Mater. 24 (2020) 167–176.

[55] H. Lin, M. Li, X. Yang, D. Yu, Y. Zeng, C. Wang, G. Chen, F. Du, Nanosheets-assembled CuSe crystal pillar as a stable and high-power anode for sodium-ion and potassium-ion batteries, Adv. Energy Mater. 9 (2019), 1900323.

[56] H. Wu, Q. Yu, C.-Y. Lao, M. Qin, W.A. Wang, Z. Liu, C. Man, L. Wang, B. Jia, X. Qu, Scalable synthesis of VN quantum dots encapsulated in ultralarge pillared N-doped mesoporous carbon microsheets for superior potassium storage, Energy Storage Mater. 18 (2019) 43–50.

[57] J. Qian, X. Wu, Y. Cao, X. Ai, H. Yang, High capacity and rate capability of amorphous phosphorus for sodium ion batteries, Angew. Chem. Int. Ed. 52 (2013) 4633–4636.

[58] Y. Kim, Y. Park, A. Choi, N.S. Choi, J. Kim, J. Lee, J.H. Ryu, S.M. Oh, K.T. Lee, An amorphous red phosphorus/carbon composite as a promising anode material for sodium ion batteries, Adv. Mater. 25 (2013) 3045–3049.

[59] J. Song, Z. Yu, M.L. Gordin, S. Hu, R. Yi, D. Tang, T. Walter, M. Regula, D. Choi, X. Li, A. Manivannan, D. Wang, Chemically bonded phosphorus/graphene hybrid as a high performance anode for sodium-ion batteries, Nano Lett. 14 (2014) 6329–6335.

[60] Y. Sun, L. Wang, Y. Li, Y. Li, H.R. Lee, A. Pei, X. He, Y. Cui, Design of red phosphorus nanostructured electrode for fast-charging lithium-ion batteries with high energy density, Joule 3 (2019) 1080–1093.

[61] Y. Liu, Q. Liu, C. Jian, D. Cui, M. Chen, Z. Li, T. Li, T. Nilges, K. He, Z. Jia, C. Zhou, Red-phosphorus-impregnated carbon nanofibers for sodium-ion batteries and liquefaction of red phosphorus, Nat. Commun. 11 (2020) 2520.

[62] Y. Fu, Q. Wei, G. Zhang, S. Sun, Advanced phosphorus-based materials for lithium/sodium-ion batteries: recent developments and future perspectives, Adv. Energy Mater. 8 (2018), 1703058.

[63] F. Yang, H. Gao, J. Chen, Z. Guo, Phosphorus-based materials as the anode for sodium-ion batteries, Small Methods 1 (2017), 1700216.

[64] Y. Wu, H.-B. Huang, Y. Feng, Z.-S. Wu, Y. Yu, The promise and challenge of phosphorus-based composites as anode materials for potassium-ion batteries, Adv. Mater. 31 (2019), 1901414.

[65] W. Zhang, J. Mao, S. Li, Z. Chen, Z. Guo, Phosphorus-based alloy materials for advanced potassium-ion battery anode, J. Am. Chem. Soc. 139 (2017) 3316–3319.

[66] X. Wu, W. Zhao, H. Wang, X. Qi, Z. Xing, Q. Zhuang, Z. Ju, Enhanced capacity of chemically bonded phosphorus/carbon composite as an anode material for potassium-ion batteries, J. Power Sources 378 (2018) 460–467.

[67] I. Sultana, M.M. Rahman, T. Ramireddy, Y. Chen, A.M. Glushenkov, High capacity potassium-ion battery anodes based on black phosphorus, J. Mater. Chem. A 5 (2017) 23506–23512.

[68] W. Xiao, Q. Sun, M.N. Banis, B. Wang, J. Liang, A. Lushington, R. Li, X. Li, T.-K. Sham, X. Sun, Unveiling the interfacial instability of the phosphorus/carbon anode for sodium-ion batteries, ACS Appl. Mater. Interfaces 11 (2019) 30763–30773.

[69] W. Xiao, Q. Sun, M.N. Banis, B. Wang, W. Li, M. Li, A. Lushington, R. Li, X. Li, T. K. Sham, X. Sun, Understanding the Critical Role of Binders in Phosphorus/Carbon Anode for Sodium-Ion Batteries through Unexpected Mechanism, Adv. Funct. Mater. 30 (2020), 2000060.

[70] W.-C. Chang, J.-H. Wu, K.-T. Chen, H.-Y. Tuan, Red phosphorus potassium-ion battery anodes, Adv. Sci. 6 (2019), 1801354.

[71] J. Bai, B. Xi, H. Mao, Y. Lin, X. Ma, J. Feng, S. Xiong, One-step construction of N, P-codoped porous carbon sheets/CoP hybrids with enhanced lithium and potassium storage, Adv. Mater. 30 (2018), 1802310.

[72] Q. Liu, Z. Hu, Y. Liang, L. Li, C. Zou, H. Jin, S. Wang, H. Lu, Q. Gu, S.L. Chou, Y. Liu, S.X. Dou, Facile synthesis of hierarchical hollow CoP@C composites with superior performance for sodium and potassium storage, Angew. Chem. Int. Ed. 59 (2020) 5159–5164.

[73] Q. Tan, W. Zhao, K. Han, P. Li, W.A. Wang, D. He, Z. Liu, Q. Yu, M. Qin, X. Qu, The multi-yolk/shell structure of FeP@foam-like graphenic scaffolds: strong P–C bonds and electrolyte- and binder-optimization boost potassium storage, J. Mater. Chem. A 7 (2019) 15673–15682.

[74] W. Li, B. Yan, H. Fan, C. Zhang, H. Xu, X. Cheng, Z. Li, G. Jia, S. An, X. Qiu, FeP/C composites as an anode material for K-ion batteries, ACS Appl. Mater. Interfaces 11 (2019) 22364–22370.

[75] F. Yang, H. Gao, J. Hao, S. Zhang, P. Li, Y. Liu, J. Chen, Z. Guo, Yolk–shell structured FeP@C nanoboxes as advanced anode materials for rechargeable lithium-/potassium-ion batteries, Adv. Funct. Mater. 29 (2019), 1808291.

[76] W. Zhang, Z. Wu, J. Zhang, G. Liu, N.-H. Yang, R.-S. Liu, W.K. Pang, W. Li, Z. Guo, Unraveling the effect of salt chemistry on long-durability high-phosphorus-concentration anode for potassium ion batteries, Nano Energy 53 (2018) 967–974.

[77] D. Li, Y. Zhang, Q. Sun, S. Zhang, Z. Wang, Z. Liang, P. Si, L. Ci, Hierarchically porous carbon supported Sn_4P_3 as a superior anode material for potassium-ion batteries, Energy Storage Mater. 23 (2019) 367–374.

[78] W. Zhang, W.K. Pang, V. Sencadas, Z. Guo, Understanding high-energy-density Sn_4P_3 anodes for potassium-ion batteries, Joule 2 (2018) 1534–1547.

[79] R. Verma, P.N. Didwal, H.-S. Ki, G. Cao, C.-J. Park, SnP_3/carbon nanocomposite as an anode material for potassium-ion batteries, ACS Appl. Mater. Interfaces 11 (2019) 26976–26984.

[80] C. Lin, L. Ouyang, C. Zhou, R. Hu, L. Yang, X. Yang, H. Shao, M. Zhu, A novel selenium-phosphorous amorphous composite by plasma assisted ball milling for high-performance rechargeable potassium-ion battery anode, J. Power Sources 443 (2019), 227276.

[81] B. Li, Z. He, J. Zhao, W. Liu, Y. Feng, Advanced Se_3P_4@C anode with exceptional cycling life for high performance potassium-ion batteries, Small 16 (2020), 1906595.

[82] L. Wang, X. He, J. Li, W. Sun, J. Gao, J. Guo, C. Jiang, Nano-structured phosphorus composite as high-capacity anode materials for lithium batteries, Angew. Chem. Int. Ed. 51 (2012) 9034–9037.

[83] Y. Zhu, Y. Wen, X. Fan, T. Gao, F. Han, C. Luo, S.-C. Liou, C. Wang, Red phosphorus–single-walled carbon nanotube composite as a superior anode for sodium ion batteries, ACS Nano 9 (2015) 3254–3264.

[84] W. Li, Z. Yang, M. Li, Y. Jiang, X. Wei, X. Zhong, L. Gu, Y. Yu, Amorphous red phosphorus embedded in highly ordered mesoporous carbon with superior lithium and sodium storage capacity, Nano Lett. 16 (2016) 1546–1553.

[85] H. Gao, T. Zhou, Y. Zheng, Y. Liu, J. Chen, H. Liu, Z. Guo, Integrated carbon/red phosphorus/graphene aerogel 3D architecture via advanced vapor-redistribution for high-energy sodium-ion batteries, Adv. Energy Mater. 6 (2016), 1601037.

[86] C. Zhang, X. Wang, Q. Liang, X. Liu, Q. Weng, J. Liu, Y. Yang, Z. Dai, K. Ding, Y. Bando, J. Tang, D. Golberg, Amorphous phosphorus/nitrogen-doped graphene paper for ultrastable sodium-ion batteries, Nano Lett. 16 (2016) 2054–2060.

[87] W. Li, S. Hu, X. Luo, Z. Li, X. Sun, M. Li, F. Liu, Y. Yu, Confined Amorphous Red Phosphorus in MOF-Derived N-Doped Microporous Carbon as a Superior Anode for Sodium-Ion Battery, Adv. Mater. 29 (2017), 1605820.

[88] S. Yao, J. Cui, J. Huang, J.-Q. Huang, W.G. Chong, L. Qin, Y.-W. Mai, J.-K. Kim, Rational assembly of hollow microporous carbon spheres as P hosts for long-life sodium-ion batteries, Adv. Energy Mater. 8 (2018), 1702267.

[89] T. Yuan, J. Ruan, C. Peng, H. Sun, Y. Pang, J. Yang, Z.-F. Ma, S. Zheng, 3D red phosphorus/sheared CNT sponge for high performance lithium-ion battery anodes, Energy Storage Mater. 13 (2018) 267–273.

[90] X. Huang, D. Liu, X. Guo, X. Sui, D. Qu, J. Chen, Phosphorus/carbon composite anode for potassium-ion batteries: insights into high initial coulombic efficiency and superior cyclic performance, ACS Sustain. Chem. Eng. 6 (2018) 16308–16314.

[91] D. Liu, X. Huang, D. Qu, D. Zheng, G. Wang, J. Harris, J. Si, T. Ding, J. Chen, D. Qu, Confined phosphorus in carbon nanotube-backboned mesoporous carbon as superior anode material for sodium/potassium-ion batteries, Nano Energy 52 (2018) 1–10.

[92] H. Wang, L. Wang, L. Wang, Z. Xing, X. Wu, W. Zhao, X. Qi, Z. Ju, Q. Zhuang, Phosphorus particles embedded in reduced graphene oxide matrix to enhance

capacity and rate capability for capacitive potassium-ion storage, Chem. Eur. J. 24 (2018) 13897–13902.
[93] P. Xiong, P. Bai, S. Tu, M. Cheng, J. Zhang, J. Sun, Y. Xu, Red phosphorus nanoparticle@3D interconnected carbon nanosheet framework composite for potassium-ion battery anodes, Small 14 (2018), 1802140.
[94] Y. Wu, S. Hu, R. Xu, J. Wang, Z. Peng, Q. Zhang, Y. Yu, Boosting potassium-ion battery performance by encapsulating red phosphorus in free-standing nitrogen-doped porous hollow carbon nanofibers, Nano Lett. 19 (2019) 1351–1358.
[95] X. Huang, X. Sui, W. Ji, Y. Wang, D. Qu, J. Chen, From phosphorus nanorods/C to yolk–shell P@hollow C for potassium-ion batteries: high capacity with stable cycling performance, J. Mater. Chem. A 8 (2020) 7641–7646.
[96] B. Liu, Q. Zhang, L. Li, Z. Jin, C. Wang, L. Zhang, Z.-M. Su, Encapsulating red phosphorus in ultralarge pore volume hierarchical porous carbon nanospheres for lithium/sodium-ion half/full batteries, ACS Nano 13 (2019) 13513–13523.
[97] C. Marino, A. Debenedetti, B. Fraisse, F. Favier, L. Monconduit, Activated-phosphorus as new electrode material for Li-ion batteries, Electrochem. Commun. 13 (2011) 346–349.
[98] C. Marino, L. Boulet, P. Gaveau, B. Fraissea, L. Monconduit, Nanoconfined phosphorus in mesoporous carbon as an electrode for Li-ion batteries: performance and mechanism, J. Mater. Chem. 22 (2012) 22713–22720.
[99] X. Liang, C. Chang, W. Guo, X. Jiang, C. Xiong, X. Pu, Red phosphorus/onion-like mesoporous carbon composite as high-performance anode for sodium-ion battery, ChemElectroChem 6 (2019) 5721–5727.
[100] J. Sun, H.-W. Lee, M. Pasta, Y. Sun, W. Liu, Y. Li, H.R. Lee, N. Liu, Y. Cui, Carbothermic reduction synthesis of red phosphorus-filled 3D carbon material as a high-capacity anode for sodium ion batteries, Energy Storage Mater. 4 (2016) 130–136.
[101] W. Xiao, Q. Sun, J. Liu, B. Xiao, P.-A. Glans, J. Li, R. Li, J. Guo, W. Yang, T.-K. Sham, X. Sun, Utilizing the full capacity of carbon black as anode for Na-ion batteries via solvent co-intercalation, Nano Res. 10 (2017) 4378–4387.
[102] W. Xiao, Q. Sun, J. Liu, B. Xiao, Y. Liu, P.-A. Glans, J. Li, R. Li, X. Li, J. Guo, W. Yang, T.-K. Sham, X. Sun, Boosting the sodium storage behaviors of carbon materials in ether-based electrolyte through the artificial manipulation of microstructure, Nano Energy 66 (2019), 104177.
[103] W. Xiao, Q. Sun, J. Liu, B. Xiao, X. Li, P.-A. Glans, J. Li, R. Li, X. Li, J. Guo, W. Yang, T.-K. Sham, X. Sun, Engineering surface oxygenated functionalities on commercial carbon toward ultrafast sodium storage in ether-based electrolytes, ACS Appl. Mater. Interfaces 12 (2020) 37116–37127.
[104] W. Li, Z. Yang, Y. Jiang, Z. Yu, L. Gu, Y. Yu, Crystalline red phosphorus incorporated with porous carbon nanofibers as flexible electrode for high performance lithium-ion batteries, Carbon 78 (2014) 455–462.
[105] B. Ruan, J. Wang, D. Shi, Y. Xu, S. Chou, H. Liu, J. Wang, A phosphorus/N-doped carbon nanofiber composite as an anode material for sodium-ion batteries, J. Mater. Chem. A 3 (2015) 19011–19017.
[106] Y. Wu, Z. Liu, X. Zhong, X. Cheng, Z. Fan, Y. Yu, Amorphous red phosphorus embedded in sandwiched porous carbon enabling superior sodium storage performances, Small 14 (2018), 1703472.
[107] K. Xu, Electrolytes and interphases in Li-ion batteries and beyond, Chem. Rev. 114 (2014) 11503–11618.
[108] D. Peng, Y. Chen, H. Ma, L. Zhang, Y. Hu, X. Chen, Y. Cui, Y. Shi, Q. Zhuang, Z. Ju, Enhancing the cycling stability by tuning the chemical bonding between phosphorus and carbon nanotubes for potassium-ion battery anodes, ACS Appl. Mater. Interfaces 12 (2020) 37275–37284.
[109] B. Li, S. Shang, J. Zhao, D.M. Itkis, X. Jiao, C. Zhang, Z.-K. Liu, J. Song, Metastable trigonal SnP: a promising anode material for potassium-ion battery, Carbon 168 (2020) 468–474.
[110] Y. Wu, H. Zhao, Z. Wu, L. Yue, J. Liang, Q. Liu, Y. Luo, S. Gao, S. Lu, G. Chen, X. Shi, B. Zhong, X. Guo, X. Sun, Rational design of carbon materials as anodes for potassium-ion batteries, Energy Storage Mater. 34 (2021) 483–507.
[111] Z. Li, Y. Zheng, Q. Liu, Y. Wang, D. Wang, Z. Li, P. Zheng, Z. Liu, Recent advances in nanostructured metal phosphides as promising anode materials for rechargeable batteries, J. Mater. Chem. A 8 (2020) 19113–19132.
[112] K. Song, C. Liu, L. Mi, S. Chou, W. Chen, C. Shen, Recent progress on the alloy-based anode for sodium-ion batteries and potassium-ion batteries, Small (2019), 1903194.
[113] P.R. Bandaru, H. Yamada, R. Narayanan, M. Hoefer, Charge transfer and storage in nanostructures, Mater. Sci. Eng. R Rep. 96 (2015) 1–69.
[114] J. Liu, J. Wang, C. Xu, H. Jiang, C. Li, L. Zhang, J. Lin, Z.X. Shen, Advanced energy storage devices: basic principles, analytical methods, and rational materials design, Adv. Sci. 5 (2017), 1700322.
[115] S. Fleischmann, J.B. Mitchell, R. Wang, C. Zhan, D.-e. Jiang, V. Presser, V. Augustyn, Pseudocapacitance: from fundamental understanding to high power energy storage materials, Chem. Rev. 120 (2020) 6738–6782.
[116] F. Yu, T. Huang, P. Zhang, Y. Tao, F.-Z. Cui, Q. Xie, S. Yao, F. Wang, Design and synthesis of electrode materials with both battery-type and capacitive charge storage, Energy Storage Mater. 22 (2019) 235–255.
[117] C. Costentin, J.-M. Savéant, Energy storage: pseudocapacitance in prospect, Chem. Sci. 10 (2019) 5656–5666.
[118] A. Eftekhari, M. Mohamedi, Tailoring pseudocapacitive materials from a mechanistic perspective, Mater. Today Energy 6 (2017) 211–229.
[119] V. Augustyn, P. Simon, B. Dunn, Pseudocapacitive oxide materials for high-rate electrochemical energy storage, Energy Environ. Sci. 7 (2014) 1597–1614.
[120] B.E. Conway, Transition from "supercapacitor" to "battery" behavior in electrochemical energy storage, J. Electrochem. Soc. 138 (1991) 1539–1548.
[121] B.E. Conway, W.G. Pell, Double-layer and pseudocapacitance types of electrochemical capacitors and their applications to the development of hybrid devices, J. Solid State Electrochem. 7 (2003) 637–644.
[122] T. Brezesinski, J. Wang, S.H. Tolbert, B. Dunn, Ordered mesoporous α-MoO_3 with iso-oriented nanocrystalline walls for thin-film pseudocapacitors, Nat. Mater. 9 (2010) 146–151.
[123] J. Come, V. Augustyn, J.W. Kim, P. Rozier, P.-L. Taberna, P. Gogotsi, J.W. Long, B. Dunn, P. Simon, Electrochemical kinetics of nanostructured Nb_2O_5 electrodes, J. Electrochem. Soc. 161 (2014) A718–A725.
[124] J.B. Cook, H.S. Kim, Y. Yan, J.S. Ko, S. Robbennolt, B. Dunn, S.H. Tolbert, Mesoporous MoS_2 as a transition metal dichalcogenide exhibiting pseudocapacitive Li and Na-ion charge storage, Adv. Energy Mater. 6 (2016), 1501937.
[125] R. Jain, P. Hundekar, T. Deng, X. Fan, Y. Singh, A. Yoshimura, V. Sarbada, T. Gupta, A.S. Lakhnot, S.O. Kim, C. Wang, N. Koratkar, Reversible alloying of phosphorene with potassium and its stabilization using reduced graphene oxide buffer layers, ACS Nano 13 (2019) 14094–14106.
[126] K.-T. Chen, H.-Y. Tuan, Bi–Sb nanocrystals embedded in phosphorus as high-performance potassium ion battery electrodes, ACS Nano 14 (2020) 11648–11661.
[127] X. Meng, X.Q. Yang, X. Sun, Emerging applications of atomic layer deposition for lithium-ion battery studies, Adv. Mater. 24 (2012) 3589–3615.
[128] X. Meng, Atomic-scale surface modifications and novel electrode designs for high-performance sodium-ion batteries via atomic layer deposition, J. Mater. Chem. A 5 (2017) 10127–10149.
[129] Y. Zhao, X. Sun, Molecular layer deposition for energy conversion and storage, ACS Energy Lett. 3 (2018) 899–914.
[130] Y. Zhao, L.V. Goncharova, Q. Zhang, P. Kaghazchi, Q. Sun, A. Lushington, B. Wang, R. Li, X. Sun, Inorganic–organic coating via molecular layer deposition enables long life sodium metal anode, Nano Lett. 17 (2017) 5653–5659.